International Journal of Mechanical Sciences 159 (2019) 467–486

Contents lists available at ScienceDirect

International Journal of Mechanical Sciences

journal homepage: www.elsevier.com/locate/ijmecsci

A new material model for thermo-mechanical analysis of steels in fire

Mian Zhou*, Rui P.R. Cardoso, Hamid Bahai

Department of Mechanical and Aerospace Engineering, Brunel University London, Kingston Lane, Uxbridge, UB8 3PH, UK

ARTICLE INFO

Keywords:
Combined isotropic-kinematic hardening
Thermo-mechanical analysis
Modelling of steels in fire

ABSTRACT

Recently developed multi-hazard frameworks for performance based engineering require material models capable of incorporating the unloading/reloading of structural materials at elevated temperatures. These include models for fire-following-earthquake events and the travelling fire methodology (which highlighted the prevalence of material's unloading/reloading). This paper proposes a new combined isotropic-kinematic hardening material model that has been developed to assess the unloading/loading behaviour of steel materials for thermo-mechanical analysis with fire, accounting for the Bauschinger effect and transient hardening behaviour. It works within the classical rate independent plasticity framework by exploiting the latitude of the two yield-surface model. The proposed material model integrates temperature effects on the yield surfaces through the concept of a shrinking/expanding bounding surface, and on the Bauschinger effect using an exponential growth function of plastic internal variables (PIVs). Transient hardening behaviour is modelled by incorporating a second non-linear kinematic hardening variable using an exponential decay function of the PIVs, and a corresponding discrete memory parameter tracks any abrupt changes in the direction of plastic loading. Describing the Bauschinger effect and its associated transient hardening behaviour using an opposite pair of exponential functions is a novel solution that simplifies the computing effort required by classical material models developed purposefully for cyclic loading. Hence it makes the proposed material model appropriate and efficient for structural analysis with fire. The proposed material model has been implemented in Abaqus using the Umat subroutine, and verified against experimental data where good agreement was observed. Its application in analysing structures subjected to complex, realistic building fire is also demonstrated, indicating that it is suitable for incorporating within performance based engineering frameworks for structures in fire.

1. Introduction

Structural material behaviour in building fire can be extremely complex due to already complicated thermal loading further compounded by intricate modern architectural design. Very sophisticated material models can be developed to analyse various phenomena for steel materials under fire using the thermodynamics framework. However constructing a material model that is capable of representing every aspect of the behaviour is an enormous and yet unneeded task. A good material model is one that can solve the engineering problems efficiently within a degree of accuracy required by the proposed problem.

Three issues have been identified to be resolved by the proposed new material model for performing finite element analysis of structural systems subjected to fire:

1. The unloading/reloading of the material during the heating stage of a building fire event. It is a conventional assumption that in structural fire design the strain will only increase monotonically during the heating phase of a fire with no strain reversal expected [1], largely established based on the behaviour of single structural elements tested in a standard fire furnace [2]. However, such assumption is no longer valid for performance based fire structural design where global structural analysis in fire is used, during which loading/unloading/reloading will inevitably occur in certain parts of the structure due to load redistribution. For instance, consider the following scenarios:
   (a) When appraising structural fire performance of buildings in a seismic zone, where plastic strains induced by historical earthquakes have to be taken into account.
   (b) With the continuous development of travelling fire methodology framework [3–5], which accounts for the movement of fire, Dai et al. [6] have demonstrated that structures will experience cross-sectional temperature gradient reversals and 'cyclic' heating and cooling during the course of a fire development.
   (c) Load redistribution between structural components through catenary action. Especially for the structural beams that experiencing large deflection in fire, the catenary action significantly influences their behaviour. A phenomenon has been observed in

* Corresponding author.
E-mail address: mian.zhou@brunel.ac.uk (M. Zhou).

https://doi.org/10.1016/j.ijmecsci.2019.05.007
Received 19 February 2019; Received in revised form 2 May 2019; Accepted 5 May 2019
Available online 9 May 2019

real fire event – Broadgate phase 8 fire [7] and in the large scale Cardington frame fire tests [8].

2. The non-linear stress strain relationships at elevated temperatures, where the non-linear stress strain behaviour of steel materials such as structural carbon steels and stainless steels have to be represented properly using appropriate strain hardening law. The material non-linearity is regarded as a norm in other engineering fields. But it is not commonly modelled in structural engineering design, largely attributed to the perfect elastic-plastic behaviour that structural carbon steels exhibit favourably at room temperature. Limited research [9] has been carried out studying the impact of the structural fire performance of stainless steels as a result of their higher material non-linearity.
3. The Bauschinger effect, the translation of the yield surface in the stress space, and its associated transient hardening behaviour at elevated temperatures. For capacity analysis of steel structures, when reverse loading occurs, a material model with the Bauschinger effect properly accounted for should be used [10,11]. Multiple experimental results [12–14] have shown the yield surfaces of metals both expand and translate at elevated temperatures. Lissenden et al. [12] measured the subsequent yield surface of 316 stainless steel at 650 °C and found that it had translated and elongated in the direction of preloading. The same translation and distortion of subsequent yield surfaces have also been observed in aluminium after being heated to 152 °C [13,14]. Furthermore, it has been observed that the Bauschinger effect is temperature dependent [13,15–17]. A diminishing trend of the Bauschinger effect at rising temperatures (21 °C, 66 °C, 108 °C and 152 °C) was observed in [13]. Harvey et al. [15] investigated the evolution of the isotropic hardening variable and kinematic hardening variable of 304L stainless steel at temperature level 20 °C, 200 °C, 600 °C, 800 °C and 1000 °C using reverse yield experiments, and demonstrated the temperature-dependent nature of the Bauschinger effect. When investigating material's kinematic hardening behaviour under cyclic loading at high temperatures, Maciejewski et al. [16] and Ohno et al. [17] observed different degrees of the Bauschinger effect and transient hardening at varying temperatures for low carbon steel and 304 stainless steel respectively.

Franssen [18] proposed that the constitutive material model for steels at elevated temperatures could be constructed by using the plastic strain to describe the complete stress strain history at varying temperatures. This approach has been implemented in finite element software SAFIR [19] for Eurocode 3 [20] steel materials with an elliptical curve adopted for the non-linear isotropic hardening behaviour [21], and also implement in the uniaxial material model Steel01Thermal in OpenSEEs [22] with the non-linear stress strain relation being simplified into a tri-linear relationship. The main shortcomings of this model are its inability to deal with multiple strain reversals and to properly account for the Bauschinger effect and transient hardening behaviour.

The above review indicates that the proposed material model should have the following capabilities:

1. Handle non-monotonic loading path;
2. Model material non-linearity at elevated temperatures;
3. Include the Bauchinger effect and transient hardening behaviour at elevated temperatures.

It is well known that the theory of plasticity provides the framework for the continuum constitutive descriptions of the behaviour of solids that experience permanent plastic deformations. The rate independent plasticity theory is restricted to the conditions for which the permanent deformations do not depend on the rate of the loading applied. Several rate independent plasticity models have been developed using the rate independent plasticity framework with internal variable concept to model the non-linear strain hardening, and the complex material behaviour under non-monotonous loading such as the Bauschinger effect and transient hardening. A brief review of the existing models is given in the next section.

2. Existing kinematic hardening models at room temperature

Isotropic hardening models are adequate for proportional loading conditions where the loading increases monotonically and no unloading occurs. In order to properly represent material's response under complex non-monotonous deformation paths, it has been common to adopt kinematic hardening models. In this section, three main types of kinematic hardening models are briefly reviewed and discussed.

2.1. Mroz's multisurface model

Mroz's model [23] uses a series of linear segments to model the non-linear stress strain behaviour, i.e. instead of using a single hardening modulus for the entire stress strain curve, each discretised segment of the stress strain curve has one constant hardening modulus. In three dimensional stress space, Mroz's model can be represented by several hypersurfaces f_0, f_1, ... f_n, where f_0 is the initial yield surface, and f_1 to f_n define regions of constant hardening moduli.

On one hand, to produce a smooth non-linear curve, a large number of yield surfaces are necessary, requiring high computational power. On the other hand, the plastic moduli (E^p) under uniaxial loading of Mroz's model can be determined straightforwardly from the stress—plastic strain curve generated from uniaxial tensile tests.

2.2. Two yield-surface models

The two-surface model concept was proposed by Krieg [24] and Dafalias and Popov [25] independently in the 70s. They introduced the concept of a bounding (outer) surface and a loading (inner) surface.

Compared with the Mroz's multisurface model that defines a set of piecewise plastic moduli, the two surface model defines a continuous variation of the plastic modulus between the bounding surface and the loading surface. The non-linear hardening behaviour — smooth transition between elastic and plastic region, is realised through the relative movement of the two surfaces.

The main difference between Krieg's model, and Dafalias & Popov's model is the approach adopted for incorporating the Bauschinger effect. Krieg [24] prescribes kinematic-isotropic proportioning factors to decompose the total hardening into isotropic and kinematic hardening parts for the loading surface and the bounding surface respectively. In Dafalias & Popov's model [25], the Bauschinger effect is realised by defining the plastic hardening modulus as a function of the gap between the bounding and the loading surface.

Lee et al. [26] resolved the issue of 'overshooting', the unrealistic transient behaviour of the two yield-surface model which may occur when the material is unloaded before being reloaded to its original stress state, by only updating the hardening behaviour when reverse loading occurs for plastic deformation.

Recently, Cardoso and Yoon [27] explicitly incorporated the Bauschinger ratio in the constitutive equation of the two-surface model by defining it as an exponential function of the accumulated plastic strain ($\overline{\varepsilon^p}$).

2.3. Nonlinear kinematic hardening models

The non-linear kinematic hardening model commonly used is a generalisation of Prager's [28] and Ziegler's [29] linear kinematic hardening models. The Prager's linear kinematic hardening rule [28] assumes the yield surface translates in the direction of plastic strain increment. Ziegler [29] modified Prager's rule by assuming yield surface translates along the direction of the relative stress tensor $\boldsymbol{\eta}$:

$$\boldsymbol{\eta} = \boldsymbol{\sigma} - \boldsymbol{\beta} \tag{1}$$

where σ is Cauchy stress tensor and β is the backstress tensor.

The evolution equation for the kinematic hardening variable β can be expressed as:

$$\beta = \frac{2}{3} H \varepsilon^p \qquad \text{and} \qquad \dot{\beta} = \frac{2}{3} H \dot{\varepsilon^p} \tag{2}$$

the material constant H is the hardening modulus and ε^p is the plastic strain tensor.

For modelling material behaviour under cyclic loading, Chaboche [30,31] proposed a non-linear kinematic hardening model as expressed in Eq. (3). The backstress (β) is modelled using multiple (M) terms of non-linear kinematic hardening, with different material constants γ_i assigned for each term to allow for a more extensive strain domain and a better description of the soft transition between elasticity and the onset of plastic flow [32].

$$\dot{\beta} = \sum_{i=1}^{M} \dot{\beta}_i \qquad \dot{\beta}_i = \frac{2}{3} H_i \dot{\varepsilon^p} - \gamma_i \beta_i \dot{\overline{\varepsilon^p}} \tag{3}$$

with:

$$\dot{\overline{\varepsilon^p}} = \sqrt{\frac{2}{3} \dot{\varepsilon^p} : \dot{\varepsilon^p}} \tag{4}$$

The variable $\dot{\overline{\varepsilon^p}}$ is the accumulated plastic strain rate and γ is a material constant. The term $-\gamma \beta \dot{\overline{\varepsilon^p}}$, called the dynamic recovery term, includes the effect of saturation in the kinematic hardening model.

Chaboche's model is developed based on the non-linear kinematic hardening model firstly proposed by Armstrong and Frederick [33] in 1966. Armstrong & Frederick's model can be considered as a particular case of Chaboche's model where $M = 1$, i.e., only one dynamic recovery term is used.

Another possible improvement upon Prager's linear kinematic hardening rule is introducing non-linearity by replacing the constant kinematic hardening modulus H with a generic function of the accumulated plastic strain, $\overline{\varepsilon^p}$ [34].

$$\dot{\beta} = \frac{2}{3} H(\overline{\varepsilon^p}) \dot{\varepsilon_p} \tag{5}$$

in this case, a scalar function,

$$\overline{\beta} \equiv \overline{\beta}(\overline{\varepsilon^p}) \tag{6}$$

must be defined such that

$$H(\overline{\varepsilon^p}) = \frac{d\overline{\beta}}{d\overline{\varepsilon^p}} \tag{7}$$

defines the kinematic hardening curve. This curve can be obtained from simple uniaxial tests in a manner analogous to the determination of the hardening curve for the purely isotropic hardening model.

The models reviewed in this section are presented within the framework of small strains and applicable to the scheme of rate independent plasticity. Chaboche and Rousselier [30] demonstrated mathematically that the non-linear kinematic hardening rule can be considered as a particular case of two-surface theory where the bounding surface can only expand isotropically but cannot translate.

All of the existing kinematic hardening models reviewed focus on the mechanical aspect of the material behaviour under isothermal condition, without explicitly stating the effects of temperature and temperature changes. Thus the three issues identified at the beginning have been answered to some degree by the existing models for isothermal conditions. In order to develop an appropriate plasticity model for thermo-mechanical analysis of steel materials subjected to fire, the effects of temperature and temperature changes have to be addressed, which is discussed in the following sections.

3. Temperature effects on plasticity models

Within the framework of thermodynamics, the temperature changes in the material can result from internal heat generation and external heat source. The flame edge temperature has been observed at about 550 °C in small-scale compartment fires and the maximum temperature in a post-flashover building fire can reach 1200 °C [35]. For structural behaviour in fire analysis, the heat transfer between the material and the external fire is believed to predominate the temperature changes within the material. Thus in this work the temperature rise in the material due to plastic work can be considered negligible in comparison to that caused by the external fire. Consequently, it's considered appropriate to decouple the heat transfer analysis from the thermo-mechanical analysis for structural analysis with fire. Strictly referring to the effects induced by external fire loading, the temperature effects on the parameters and variables in the constitutive equations and evolution laws of a plasticity model are one of the main focuses in this work.

The influence of elevated temperatures on elastic and inelastic material response, can be treated within the framework of theories of creep [36] or using the viscoplasitc theory [37–39], where material response is treated as time-dependent.

For structural fire analysis, the structural loading is generally static. Experimental evidence [12] has shown that different loading rates have no significant influence on the initial yield surfaces at elevated temperatures. Sun et al. [40] and Maciejewski et al. [16] examined strain-rate sensitivity of carbon steel beams and steel-framed structures subjected to elevated temperatures using the Chaboche and Rousselier's viscoplastic model [30]. Both [16,40] concluded that the strain rate dependency only becomes noticeable when the temperature goes beyond material's transitional temperature, about 700 °C for low carbon steel.

For steel structural fire design, Eurocode 3 (EC 3) [20] implicitly includes the effects of transient thermal creep in its prescribed stress strain curves. Material models constructed based on the EC 3 stress strain curves are applicable for heating rates between 2 and 50K/min, without the need to explicitly consider transient thermal creep [20].

Hence a time-independent/rate independent plasticity model is assumed to be adequate for the structural fire analysis, as both strain rate and creep have been demonstrated to be insignificant for structural steel material's behaviour at elevated temperature. The influence of temperature and temperature changes within the framework of rate independent plasticity model is investigated and discussed in the following sections.

3.1. Parametric dependency on temperature

The material parameters in the constitutive equations are considered to be temperature dependent. For structural steel materials, e.g. carbon steel and stainless steel, structural design standards such as EC 3 [20] provide reduction factors of elastic modulus, yield stress (proportional limit stress) and 0.2% proof stress at elevated temperatures 20–1200 °C, with 100 °C intervals. The plastic modulus can be determined using the uniaxial stress strain curves at elevated temperatures found in design standards and literature. For example, EC3 [20] provides formulas for determining the stress strain relationships of structural steels using its corresponding reduction factors.

3.2. Temperature rate dependency for the internal variables

The most commonly adopted two internal state variables to be considered are the accumulated plastic strain $\overline{\varepsilon_n^p}$ and the backstress tensor β. The scalar $\overline{\varepsilon_n^p}$ defines the isotropic hardening of the Von Mises yield surface, while the tensor β defines the translation of the yield surface centre in the deviatoric stress space.

The evolution of β at elevated temperatures has been a subject of discussion for decades and the inclusion of a temperature rate is considered necessary for obtaining stable conditions [32]. Using the framework of thermodynamics with decoupled heat transfer, considering only the kinematic hardening of the material, the thermodynamic potential, or the Helmholtz free energy (ψ) can be defined as follows:

$$\psi = \psi_e(\varepsilon^e, T) + \psi_p(\alpha, T) \tag{8}$$

The $\boldsymbol{\alpha}$ is the backstrain tensor. In this work Eq. (8) considers no internal heat generated by plastic work. Thus the ψ_p does not contribute to the heat transfer analysis in the proposed material model where the heat transfer is decoupled from the thermo-mechanical analysis. If the part ψ_p of the Helmholtz free energy is expressed in a quadratic form as:

$$\psi_p(\boldsymbol{\alpha}) = \frac{1}{3} H(T)\boldsymbol{\alpha} : \boldsymbol{\alpha} \tag{9}$$

where the hardening modulus (H) is now a function of temperature. Then the corresponding backstress is given by:

$$\boldsymbol{\beta} = \frac{\partial \psi}{\partial \boldsymbol{\alpha}} = \frac{2}{3} H(T)\boldsymbol{\alpha} \tag{10}$$

Differentiating Eq. (10) over temperature gives:

$$\frac{\partial \boldsymbol{\beta}}{\partial T} = \frac{2}{3} H(T)\frac{\partial \boldsymbol{\alpha}}{\partial T} + \frac{2}{3}\frac{\partial H(T)}{\partial T}\boldsymbol{\alpha} \tag{11}$$

The evolution of the internal variable backstress $\boldsymbol{\beta}$ over changing temperatures can therefore be determined using Eq. (11).

4. Decoupling thermal and mechanical step

For isotropic materials, the thermal expansion caused by a change in temperature is uniform in all directions. It is an experimentally observed fact that a stress free material body will experience relative elongations but no angular changes as result of an increase or a decrease in temperature. This thermally induced strain can be imposed on the stress induced strains (mechanical strains), provided there is no change in the temperature due to the deformation of the material. Thus the total strain — a measure of the deformation of the material, consists of a mechanical part and a thermal part, which can be expressed as:

$$\varepsilon_{total} = \varepsilon_{mech} + \varepsilon_{thermal} \tag{12}$$

The stress state (σ) for the structural material (elastic or plastic) depends only on the mechanical strains, which means thermal expansion does not directly contribute to plastic yielding if there is no boundary restraint. This relationship is the most fundamental relationship that governs the thermo-mechanical behaviour of structural materials subjected to fire. Where there is no boundary restraint and no external loading, the material is free to expand resulting in changes in the deformation such as axial expansion or thermal bowing, however there is no mechanical strain developed in the material in this case, hence no change of the stress state.

$$\begin{aligned} \Delta\varepsilon_{total} &= \Delta\varepsilon_{thermal} \\ \Delta\varepsilon_{mech} &= 0 \qquad \Delta\sigma = 0 \end{aligned} \tag{13}$$

By contrast, if there is still no external loading but there exist boundary restraints that fully prevent any thermal expansion, the deformation of the structural material remains unchanged. In this case, the mechanical strains are developed, subsequently cause changes in the stress state.

$$\begin{gathered} \Delta\varepsilon_{total} = 0 \\ \Delta\varepsilon_{total} = \Delta\varepsilon_{mech} + \Delta\varepsilon_{thermal} \Rightarrow \Delta\varepsilon_{mech} + \Delta\varepsilon_{thermal} = 0 \\ \Rightarrow \Delta\varepsilon_{mech} = -\Delta\varepsilon_{thermal} \\ \Delta\sigma \neq 0 \end{gathered} \tag{14}$$

The above two scenarios represent two opposite boundary conditions in real structures under fire. It can be clearly shown that any changes in the stress state that would cause material yielding are direct results of mechanical strain development. Therefore, rate independent plasticity models developed for isothermal conditions are appropriate for modelling the mechanical aspect of the thermo-mechanical analysis of structural materials subjected to fire.

A fully thermo-mechanical analysis of structural materials in fire can be viewed as a series of isothermal mechanical analysis, each one corresponding to a thermostatic state. At each state, the isothermal mechanical analysis is carried out at the temperature related to that state.

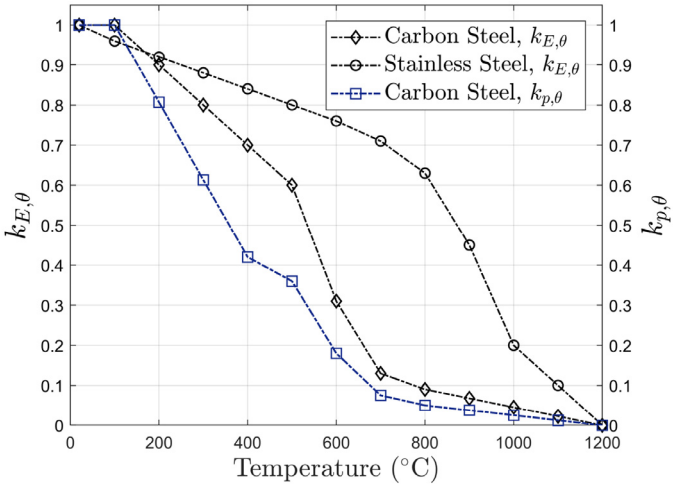

Fig. 1. Stiffness reduction factors.

The temperature difference between two neighbouring states affects the evolution of internal variables as discussed in Section 3. By adding a thermal step upon the established isothermal mechanical analysis to incorporate the temperature effects, a new material model developed within the framework of rate independent plasticity will become capable of thermo-mechanical analysis with fire.

4.1. Thermal step

The main objective of the thermal step is to implement temperature effects into the material parameters for the constitutive equations and for the evolution equations of the internal variables, thereby enabling the subsequent mechanical analysis to be performed in an isothermal state. By isolating the mechanical aspect of the analysis from any thermal effects, it allows us to take advantages of sophisticated stress integration methods developed for existing plasticity models, such as forward-Euler method incorporating sub-incrementation [41–44], midpoint method [45,46], radial return method [47–49], and backward-Euler method [50–52], in order to achieve higher computing efficiency.

The material parameters that are temperature dependent and have to be updated at the thermal step are the following:

1. Elastic modulus.
2. Yield stress, defined as occurring at proportional limit.
3. Parameters in the constitutive equation for $\boldsymbol{\epsilon^P}$, or flow rule.
4. Parameters in the evolution equations for internal variables.

4.1.1. Elastic modulus at elevated temperatures

Fig. 1 presents the reduction factors (k_E) of initial elastic modulus provided by EC 3 [20] for carbon steel and Design Manual of Structural Stainless Steel (DMSSS) [53] for stainless steel. Both steel materials exhibit reduction of stiffness at increasing temperatures.

4.1.2. Yield surfaces at elevated temperatures

The yielding, defined as occurring at the proportional limit, is temperature dependent. The initial yield surfaces at elevated temperatures shrink as temperature rises. Fig. 1 shows the reduction factors (k_p) for structural carbon steel according to EC 3 [20].

At room temperature, the yield criterion of von Mises has been shown to be in excellent agreement with experiments for many ductile metals [54]. The von Mises yield criterion predicts the initial yield surface to be a circle in the devitoric stress space. At elevated temperatures, Phillips et al. [13] experimentally determined yield surfaces of pure aluminium at 66 °C, 108 °C and 152 °C; Lissenden et al. [12] experimentally investigated the initial yield surface of type 316 stainless steel at 650 °C; Inoue

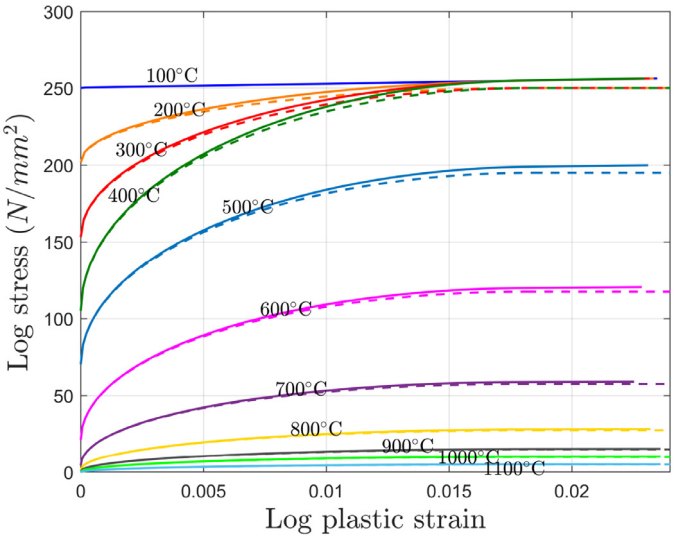

Fig. 2. EC3 stress-strain curves v.s. Least square fitting.

and Tanaka [55] carried out a series of experiments and obtained the initial yield surfaces of low carbon steel at 200 °C, 250 °C, 300 °C and 450 °C. They all found that the size and shape of experimentally determined initial yield surfaces agreed satisfactorily to that predicted using the von Mises yield criterion. Therefore, it is reasonable to believe the von Mises yield criterion remains applicable at elevated temperatures.

4.1.3. Plastic flow potential at elevated temperatures

The foundation of the plastic flow potential theory is the normality flow rule of a potential function. At higher temperatures, Lissenden et al. [12] observed that for 316 stainless steel, the directions of the plastic increment pointed in the general direction of the outward normal of the yield locus at 650 °C. It is believed that the normality is still applicable for steels at elevated temperatures. Consequently, the flow potential can be determined by the yield function and hardening law using the associated flow theory [54].

The hardening law of the carbon steel material model can be obtained by least square fitting the EC 3 [20] stress strain curves at elevated temperatures using the Voce law:

$$\sigma_{y,T} = \sigma_{y_{0,T}} + \upsilon_T * (1 - exp(-\delta_T \overline{\varepsilon_p})) \tag{15}$$

where $\sigma_{y_0,T}$ is the initial yield stress (yielding stress of proportional limit) at temperature T, which can be calculated using reduction factor (k_p) prescribed by EC 3 or determined through least square fitting the stress strain curves. The parameter ν_T and δ_T are both temperature dependant material constants. It's found that a better least square fitting results, using the Adj-R-square ratio as the indicator, could be achieved by determining $\sigma_{y_0,T}$ through curve fitting. Fig. 2 shows the carbon steel stress — plastic strain curves at elevated temperatures, with the EC 3 curves in solid line and the curves obtained using curve fitting in dashed line. A general good agreement is achieved. The material parameters obtained are summarised in Table D.1. Linear interpolation techniques are employed for obtaining the values for intermediate temperatures.

4.1.4. Internal state variables evolution at elevated temperatures

The accumulated plastic strain $(\overline{\varepsilon_n^p})$ remains constant during the thermal step. The backstress tensor $\boldsymbol{\beta}$ evolves over changing temperatures as expressed in Eq. (11).

At the thermal step where no change in the (mechanical) strain increment considered, $\frac{\partial \boldsymbol{\alpha}}{\partial T} = 0$. Eq. (11) can be reduced to:

$$\frac{\partial \boldsymbol{\beta}}{\partial T} = \frac{2}{3}\frac{\partial H(T)}{\partial T}\boldsymbol{\alpha} \tag{16}$$

Since $\boldsymbol{\beta}$ is deemed temperature rate independent, its value at a temperature point T can be determined by:

$$\boldsymbol{\beta}_T = (\boldsymbol{\beta})_{T=0} + \frac{\partial \boldsymbol{\beta}}{\partial T}T \tag{17}$$

As the tangent hardening modulus H is linearly interpolated between two stress — strain curves at different temperatures, H becomes H_T — the hardnening modulus at the temperature T, and substituting Eq. (16) into Eq. (17) gives:

$$\boldsymbol{\beta}_T = (\boldsymbol{\beta})_{T=0} + \frac{2}{3}H_T\boldsymbol{\alpha} \tag{18}$$

Eq. (18) can therefore be used to determine the new position of the yield surface centre due to a temperature change at the thermal step for the current material point position.

5. A new rate independent plasticity model for structural thermo-mechanical analysis in fire

The new rate independent plasticity model for thermo-mechanical analysis of steel materials subjected to fire developed is a combined isotropic and kinematic hardening model. It adopts the concept of yield and bounding surfaces of the two-surface plasticity theory in combination with the Bauschinger ratio to model the material's Bauschinger effect. Meanwhile, two kinematic hardening variables are used to model the transient hardening behaviour that material exhibits upon reverse loading. The theoretical details of the proposed new model are described in this section.

5.1. Thermal step

During the thermo-mechanical analysis, the thermal step is responsible for updating both the bounding and the yield surface at elevated temperatures. In the proposed material model, the bounding surface at a temperature T is considered to have isotropic hardening only, shown as dashed circles in Fig. 3. The size of the bounding surface can be obtained using the uniaxial tensile stress — plastic strain relationships combined with von Mises yield criterion, with all the material parameters at the temperature T applied. This gives the bounding surface (F = 0):

$$F_T = J(\boldsymbol{\sigma}) - \sqrt{\frac{2}{3}}Y_{1D,T}(\overline{\varepsilon^p}) = 0$$
$$J(\boldsymbol{\sigma}) = \sqrt{\boldsymbol{s} : \boldsymbol{s}} \tag{19}$$

where J represents the size of the surface in the deviatoric stress space, and $\boldsymbol{s}$ is the deviatoric stress tensor.

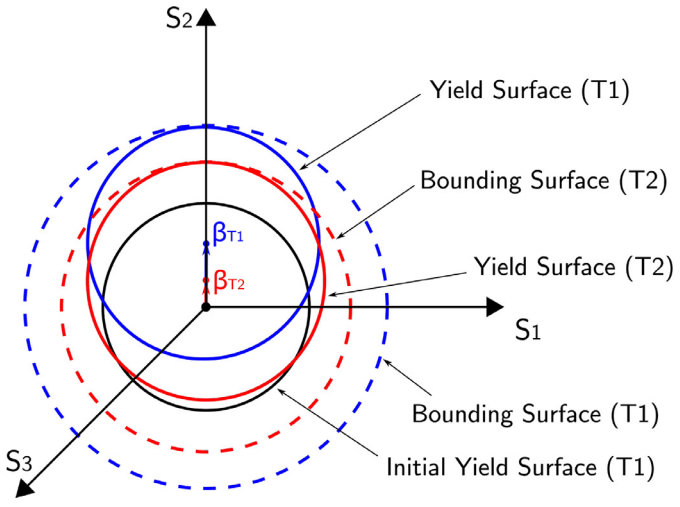

Fig. 3. Combined isotropic/kinematic hardening yield surfaces with temperature changes in the deviatoric stress space.

The (inner) yield surface ($f = 0$) can expand isotropically and move kinematically. The yielding function is defined as in Eq. (20), incorporating the Bauschinger ratio ϑ_T. With the same uniaxial stress strain curve adopted, the bounding surface and yielding surface share the same shape, as shown in Fig. 3.

$$f_T = J(\boldsymbol{\sigma} - \boldsymbol{\beta_T}) - \vartheta_T \sqrt{\frac{2}{3}} Y_{1D,T}(\overline{\varepsilon^p}) = 0$$
$$J(\boldsymbol{\sigma} - \boldsymbol{\beta_T}) = \sqrt{(\boldsymbol{s} - \boldsymbol{\beta_T}) : (\boldsymbol{s} - \boldsymbol{\beta_T})} \tag{20}$$

The Bauschinger ratio ϑ_T decomposes the size of the bounding surface at the current temperature into the isotropic hardening and the kinematic hardening part of the yield surface, and is defined by Eq. (21). At the starting point there is only isotropic hardening, $Y_{iso,T} = Y_{1D,T} \Rightarrow \vartheta_T = 1.0$.

$$\vartheta_T = \frac{Y_{iso,T}}{Y_{1D,T}}$$
$$0 \le \vartheta_T \le 1 \tag{21}$$

The evolution of Bauschinger ratio is evaluated using an exponential function of accumulated plastic strain ($\overline{\varepsilon^p}$),

$$\vartheta_T = a_T * exp(-b_T * \overline{\varepsilon^p}) + c_T \tag{22}$$

where a_T, b_T, c_T are temperature dependent material coefficients.

During thermo-mechanical analysis, the subsequent yield surfaces shrink due to the reduction in the elastic region at elevated temperature, meanwhile they also expand and translate due to the plastic hardening. As illustrated in Fig. 3, the black circle depicts the initial yield surface at temperature T1. The dashed blue circle is the bounding surface at T1 with only isotropic hardening considered. The yield surface ($f_{T1} = 0$) is the solid blue circle considering both isotropic and kinematic hardening.

At an increasing temperature T2, the bounding surface ($F_{T2} = 0$) is the red circle in dashed line. At the thermal step, since there is no (mechanical) strain increment considered, the yield surface at T2 ($f_{T2} = 0$) should not go beyond the bounding surface. The movement of the yield surface caused by the evolution of backstress due to changing temperatures should be restricted by the bounding surface.

Upon a temperature change, the backstress tensor $\boldsymbol{\beta_T}$ gives a new position of the centre of the yield surface in the deviatoric stress space, and is determined by Eq. (23). It is derived from Eq. (18) by adopting uniaxial tensile stress strain curves for the determination of hardening modulus and the Bauschinger ratio for decomposing the kinematic hardening from the total hardening.

$$\boldsymbol{\beta_T} = (1.0 - \vartheta_T)\sqrt{\frac{2}{3}} Y_{1D,T}(\overline{\varepsilon^p}) \frac{\boldsymbol{\varepsilon^p}}{\|\boldsymbol{\varepsilon^p}\|} \tag{23}$$

The re-positioning of the yielding surfaces due to temperature changes is performed at the thermal step, to allow the plastic strain increment to be determined following the established algorithms of associative plastic flow rule in the subsequent mechanical step. As illustrated in Fig. 3, the yield surface centre has to be re-positioned from $\boldsymbol{\beta}_{T1}$ to $\boldsymbol{\beta}_{T2}$.

When temperature increases from T1 to T2, S_{T1} (green dot on the blue circle in Fig. 4, which is the stress state converged at T1, now sits outside of the bounding surface of T2 (red circle in dashed line). The bounding surface size at T2 (J^*_{T2}) can be determined by Eq. (24). The Bauschinger ratio at T2 (ϑ_{T2}) determines the size of yield surface at T2 (J_{T2}) following Eq. (25) and the backstress $\overline{\beta}_{T2}$ using Eq. (26). The Bauschinger ratio ensures the yield surface always stays inside the bounding surface.

$$J^*_{T2} = \sqrt{\frac{2}{3}} Y_{1D,T2}(\overline{\varepsilon^p}) \tag{24}$$
$$J_{T2} = \vartheta_{T2} * J^*_{T2} \tag{25}$$

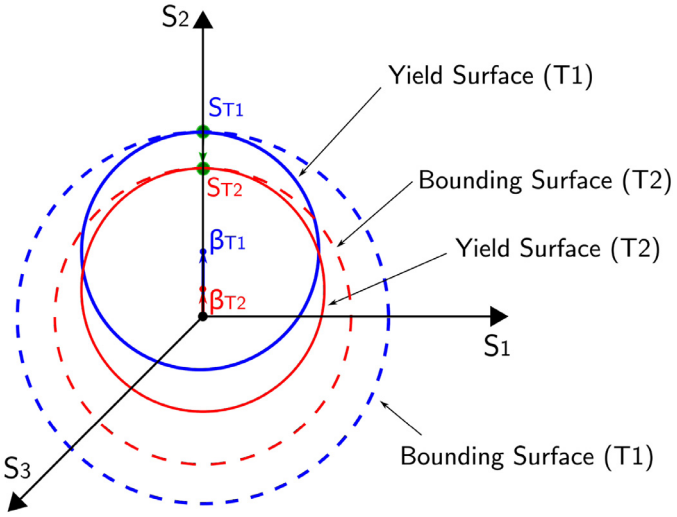

Fig. 4. Re-positioning of yield surface due to changing temperatures.

$$\overline{\beta}_{T2} = (1 - \vartheta_{T2}) * J^*_{T2} \tag{26}$$

The direction of the backstress tensor at T2 ($\boldsymbol{\beta}_{T2}$) is in the direction of the plastic strain tensor, hence the $\boldsymbol{\beta}_{T2}$ can be computed using Eq. (27):

$$\boldsymbol{\beta_{T2}} = \overline{\beta}_{T2} \frac{\boldsymbol{\varepsilon^p}}{\|\boldsymbol{\varepsilon^p}\|} \tag{27}$$

The equivalent stress state (S_{T2}) on the yield surface of T2 (green dot on the red circle in Fig. 4) can therefore be determined following Eq. (28):

$$\boldsymbol{S_{T2}} = J_{T2} \frac{\boldsymbol{\varepsilon^p}}{\|\boldsymbol{\varepsilon^p}\|} - \boldsymbol{\beta_{T2}} \tag{28}$$

As can be seen in Eqs. (27) and (28), during the thermal re-positioning, the direction of the yield surface centre and the equivalent stress state are determined by the direction of the plastic strain tensor. In the proposed material model, plastic strain tensor is considered the true PIV at the thermal step.

5.2. Mechanical step

At the mechanical step, the stress state is considered isothermal hence the temperature dependence can be deemed "frozen" during the stress integration process. The Bauschinger effect is captured by incorporating Bauschinger ratio ($\vartheta(\overline{\varepsilon^p})$) as an internal variable. The evolution function of $\vartheta(\overline{\varepsilon^p})$ is an exponential growth function of the accumulated plastic strain ($\overline{\varepsilon^p}$), thus $\vartheta(\overline{\varepsilon^p})$ is a PIV as it evolves over plastic hardening. Besides the Bauschinger effect, the material also exhibits transient hardening upon reverse loading. In the proposed model, two nonlinear kinematic hardening variables are adopted to capture these two behaviour, defined as in Eq. (29). The second variable ($\dot{\boldsymbol{\beta}}_2$) only gets activated upon reverse loading.

$$\dot{\boldsymbol{\beta}} = \dot{\boldsymbol{\beta}}_1 + \dot{\boldsymbol{\beta}}_2 * l \tag{29}$$

The internal variable — reverse loading index (l) is introduced to track any drastic changes of the loading direction. Fig. 5 shows the reverse loading can be detected by the angle θ_d between the old loading direction and the new loading direction as follows:

$$cos(\theta_d) = \frac{\boldsymbol{\eta}_{old} \cdot \boldsymbol{\eta}_{new}}{\|\boldsymbol{\eta}_{old}\| \|\boldsymbol{\eta}_{new}\|}; \qquad \boldsymbol{\eta} = \boldsymbol{s} - \boldsymbol{\beta}$$
$$cos(\theta_d) \geqslant 0, \quad l = 0; \qquad cos(\theta_d) < 0, \quad l = 1 \tag{30}$$

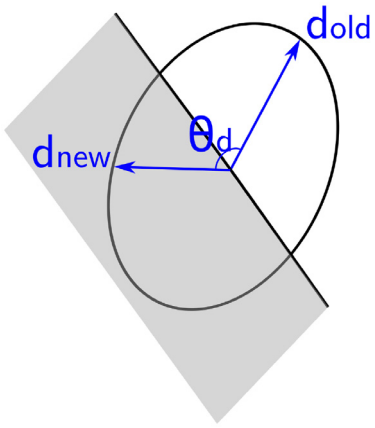

Fig. 5. Reverse loading criterion.

5.2.1. First kinematic hardening variable $\dot{\boldsymbol{\beta}}_1$

During monotonic loading, as illustrated in Fig. 6a, the first backstress term ($\dot{\boldsymbol{\beta}}_1$) accounting for the movement of the yielding surface (solid blue circle) is determined through the Bauschinger ratio ($\vartheta(\overline{\varepsilon^p})$) as follows:

$$\dot{\boldsymbol{\beta}}_1 = (1 - \dot{\vartheta}(\overline{\varepsilon^p}))\sqrt{\frac{2}{3}}\dot{Y}_{1D}(\overline{\varepsilon^p}) * \frac{\boldsymbol{\eta}}{\|\boldsymbol{\eta}\|} \tag{31}$$

Upon reverse loading, the $\dot{\boldsymbol{\beta}}_1$ continues to develop in the reverse loading direction as $\overline{\varepsilon^p}$ increases. The $\vartheta(\overline{\varepsilon^p})$ decomposes the kinematic hardening out of the total hardening at the new loading direction, illustrated as the green bracket portion of the radius of the new bounding surface (dashed green circle) in Fig. 6b.

5.2.2. Second kinematic hardening variable $\dot{\boldsymbol{\beta}}_2$

In addition to the $\dot{\boldsymbol{\beta}}_1$, a second kinematic hardening variable is introduced in the proposed model to describe the shifted yield surface centre (blue dot in Fig. 6) travelling back to the origin of the deviatoric stress space. Acknowledging the evanescent characteristic of kinematic hardening, the second variable $\dot{\boldsymbol{\beta}}_2$ can be viewed as the yield surface exhibiting an urgent tendency to move back quickly to the origin upon reversing.

The exponential growth function of Eq. (22) adopted for Bauschinger ratio evolution indicates that the yield surface moves away from the origin at an exponential speed during initial loading. It is reasonable to postulate that the yield surface exhibits the same tendency upon reversing, shifting back to the origin at an exponential rate, if not following the identical speed to that during the initial loading.

Based on this assumption, a reverse loading ratio ($\upsilon(\overline{\varepsilon_l^p})$) is introduced as an exponential decay function of the effective plastic strain of the new reloading branch, denoted $\overline{\varepsilon_l^p}$, as in Eq. (32). The scalar $\overline{\varepsilon_l^p}$ accounts for the effective plastic strain accumulated during each loading branch, and will be reset to zero whenever reverse loading is detected. The material parameter in Eq. (32) can be obtained from the testing data of reverse loading curves. Simplifying to assume the same exponential speed for the backtracking, the same material constant b in the Bauschinger ratio evolution Eq. (22) can be used, which gives:

$$\upsilon = 1.0 - exp(-b * \overline{\varepsilon_l^p}) \tag{32}$$

The typical evolution of reverse loading ratio is compared with that of Bauschinger ratio in Fig. 7. The Bauschinger ratio starts at 1.0 indicating pure isotropic hardening at the beginning of plastic hardening. It decays and steadies at a value below 1.0 where kinematic hardening has reached its saturation value. Contrarily, the reverse loading ratio starts from 0.0 meaning the backtracking is yet to start, and plateaus at the value of 1.0, indicating at this point the entire distance travelled by the yield surface centre in the previous loading branch has been recovered.

The kinematic hardening ($\dot{\boldsymbol{\beta}}_2$) is therefore defined as:

$$\dot{\boldsymbol{\beta}}_2 = \dot{\upsilon}\sqrt{\frac{2}{3}}\dot{\overline{\beta}}_l * \frac{\boldsymbol{\eta}}{\|\boldsymbol{\eta}\|} \tag{33}$$

The $\overline{\beta}_l$ is a scalar — the distance the yield surface centre travelled during the last loading branch in the uniaxial stress direction, as shown in Fig. 8, and can be obtained as follows:

$$\dot{\overline{\beta}}_l = V_h\sqrt{\frac{3}{2}\dot{\boldsymbol{\beta}}_n : \dot{\boldsymbol{\beta}}_n} \tag{34}$$

where $\dot{\boldsymbol{\beta}}_n$ is the rate of the (total) backstress tensor at the end of last loading branch prior to the start of reserve loading. The material parameter V_h is introduced to account for potential softening/hardening during reverse loading. It can be obtained using experimental reverse stress strain data.

The second variable $\dot{\boldsymbol{\beta}}_2$ gets activated upon reverse loading, more precisely only when re-yielding starts. Between the reverse loading point and the re-yielding point, shown as green dots in Fig. 8, is the unloading range during which plastic internal variables remain unchanged.

5.3. Thermal step during reverse loading

The second kinematic variable $\dot{\boldsymbol{\beta}}_2$ was introduced in Section 5.2 when describing the mechanical step of the proposed model to account for material's transient hardening behaviour during reverse loading.

The thermal step described in Section 5.1 applies to the temperature changes experienced by the internal variables during initial monotonic loading. For modelling temperature changes that occur during reverse loading, the $\dot{\boldsymbol{\beta}}_2$ has to be appropriately incorporated in the thermal step to ensure the transient behaviour is retained.

The $\dot{\boldsymbol{\beta}}_2$ describes the yield surface backtracking the distance ($\overline{\beta_l}$) that has been travelled in the stress space prior to the reverse loading. Since the distance ($\overline{\beta_l}$) is inherited from the previous loading branch, it remains constant during the reverse loading. As shown in Eq. (33), the temperature only affects the 'speed' of the $\boldsymbol{\beta}_2$ as the material parameter b in the evolution function of the reverse loading ratio (υ) is considered temperature dependent.

Therefore, the $\dot{\boldsymbol{\beta}}_2$ does not actively contribute during the thermal step. The procedures described in Section 5.1 for updating bounding surface and yield surface resulting from temperature changes can be viewed as taking place from the yield surface centre positioned at $\boldsymbol{\beta}_2$ in the stress space. Thus the algorithm proposed in Section 5.1 is still applicable, recognising that the backstress used in the algorithm exclusively refers to the first kinematic hardening variable $\boldsymbol{\beta}_1$.

The only modification required is in the last step — calculating the equivalent stress state — to take the $\boldsymbol{\beta}_2$ into account. Eq. (28) now becomes:

$$\boldsymbol{S}_{T2} = J_{T2}\frac{\boldsymbol{\varepsilon}^p}{\|\boldsymbol{\varepsilon}^p\|} - \boldsymbol{\beta}_{1_{T2}} - \boldsymbol{\beta}_2 \tag{35}$$

5.4. Elastoplastic consistent tangent modulus $\mathbf{D}^{ep}$

The exact linearisation of the incremental stress updating procedure, rather than to appeal to the rate stress — strain tangential relation, is essential for achieving quadratic rates of convergence in the iterative solution of the finite element equilibrium equations as emphasised by Negtegaal [56], Simo and Taylor [57].

Linearising the incremental constitutive function of stress tensor ($\boldsymbol{\sigma}$) yields the consistent tangent operator ($\boldsymbol{D}$).

$$\boldsymbol{D} = \frac{\partial \Delta\boldsymbol{\sigma}}{\partial \Delta\boldsymbol{\epsilon}} \tag{36}$$

The fully implicit backward-Euler return mapping algorithm has been adopted in the proposed material model to solve the yield condition equation:

$$\Phi(\Delta\gamma) \equiv \|\boldsymbol{\eta}_{n+1}^{trial}\| - 2\mu\Delta\gamma - (\overline{\beta}_{1_{n+1}} - \overline{\beta}_{1_n}) - \hat{H}(l)(\overline{\beta}_{2_{n+1}} - \overline{\beta}_{2_n}) - \sigma_{y,iso} = 0 \tag{37}$$

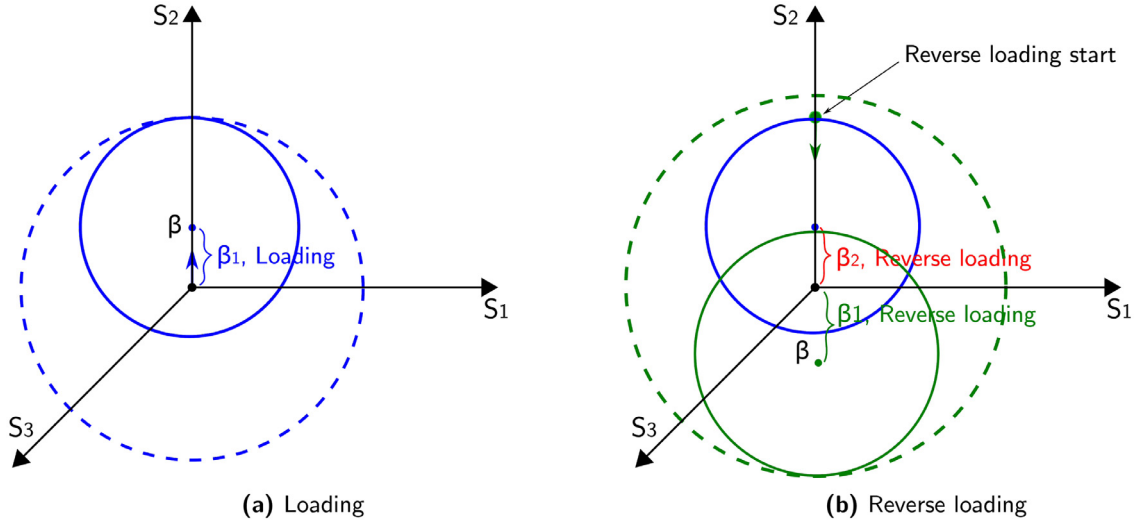

Fig. 6. Proposed model during loading — reverse loading in the deviatoric stress space.

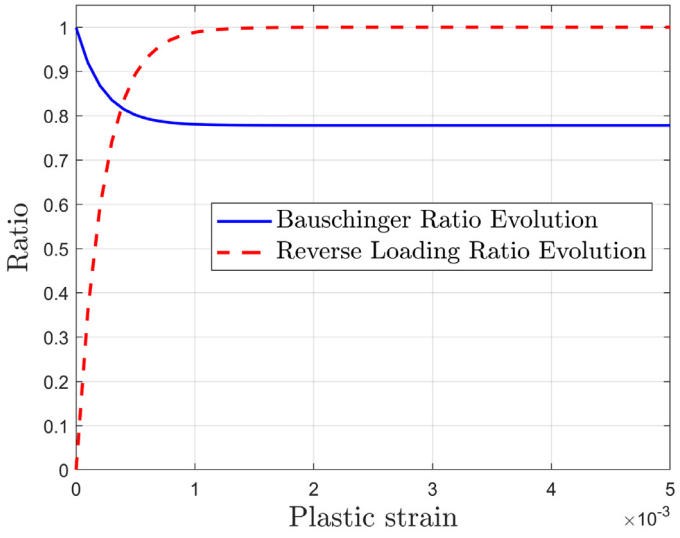

Fig. 7. Typical Bauschinger ratio and Reverse loading ratio evolution.

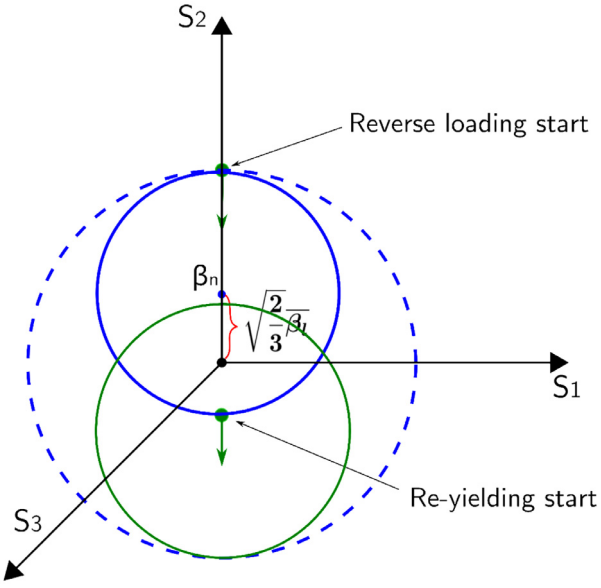

Fig. 8. Proposed model during reverse loading in the deviatoric stress space.

where $\overline{\beta_1}$ is the first kinematic term contributing to overall hardening and is a function of accumulated plastic strain ($\overline{\varepsilon^p}$) as defined in Eq. (26). $\overline{\beta_2}$ is the second kinematic hardening term defined in Eq. (33), l is the reverse loading index, and $\sigma_{y,iso}$ is the radius of the yield surface as defined in Eq. (25). $\hat{H}$ is the Heaviside step function.

Eq. (37) states the yield condition equation of full terms, using the Heaviside step function to include the second kinematic hardening term whenever reverse loading is detected. The Heaviside step function is a non-differentiable function, which means the elastoplastic consistent tangent modulus has to be derived for monotonic loading and reverse loading differently.

The elastoplastic consistent tangent during monotonic loading has been obtained as:

$$\boldsymbol{D}^{ep} = \boldsymbol{D}^{e} - 4\mu^2\Theta\boldsymbol{N}\otimes\boldsymbol{N} - \frac{4\mu^2}{\|\boldsymbol{\eta}_{n+1}^{trial}\|}[\boldsymbol{I}_{\boldsymbol{dev}} - \boldsymbol{N}\otimes\boldsymbol{N}] \tag{38}$$

$$\Theta = 2\mu + \frac{2}{3}H_{1D}(\overline{\varepsilon^p}_n + \sqrt{\frac{2}{3}}\Delta\gamma) \tag{39}$$

During reverse loading, Eq. (38) is still applicable with the term Θ modified to include the $\boldsymbol{\beta_2}$ term as follows:

$$\Theta = 2\mu + \frac{2}{3}H_{1D}\left(\overline{\varepsilon^p}_n + \sqrt{\frac{2}{3}}\Delta\gamma\right) - \frac{2}{3}\overline{\beta}_l exp\left(-b\left(\overline{\varepsilon^p}_{l\,n} + \sqrt{\frac{2}{3}}\Delta\gamma\right)\right)(-b) \tag{40}$$

The detailed derivation of elastoplastic consistent tangent modulus is provided in Appendix C.

6. Verification of evolution of isotropic & kinematic hardening variable during monotonic loading

In the thermo-mechanical analysis, the parameters in the evolution function of Bauschinger ratio becomes temperature dependant. The main objective of this section is to verify the evolution of the Bauschinger ratio in the proposed material model as a function of accumulation plastic strain ($\overline{\varepsilon^p}$) in conjunction with temperature.

Harley et al. [15] conducted a series of reverse yield experiments to measure the evolution of isotropic hardening variable (κ) and kinematic hardening variable ($\overline{\beta}_{11}$) in 304L stainless steel over a range of temperatures. The scalar isotropic hardening variable κ is related to the size of a rate independent yield surface. The $\overline{\beta}_{11}$ is associated with the translation of the yield surface centre in the uniaxial stress direction. The experimental observations of Harley et al. [15] are consistent with the combined isotropic/kinematic hardening framework. Despite their inability to directly capture the initial elastic unloading behaviour in the reverse yield experiments largely due to the inelastic material behaviour of 304L stainless steel, they determined the parameters by correlating the data from additional Large Strain Reverse (LSR) experiments and the tensile segment of the reverse yield experiments.

Harley et al.'s [15] data provided us an insight into how Bauschinger effect evolves at elevated temperatures, particularly into how the two internal variables (κ and $\overline{\beta}_{11}$) of a combined isotropic/kinematic hardening plasticity model evolve at elevated temperatures.

In this verification study, at first, the κ and $\overline{\beta}_{11}$ results of Harley et al.'s experiments were analysed, based on which a set of temperature dependent evolution function parameters of the Bauschinger ratio were determined using the least square fitting technique. The parameters determined were implemented in the proposed material model for thermo-mechanical analysis in Abaqus using the Umat subroutine [58]. The verification was performed by comparing Abaqus results with the experimental data.

6.1. Bauschinger effect determination at elevated temperatures

Based on the uniaxial stress state of the reverse yield experiment in [15], neglecting the term for rate dependence in yield strength, the Bauschinger ratio (ϑ) can be determined following:

$$\begin{aligned} \sigma_{11} &= \kappa + \beta_{11} \\ \vartheta &= \frac{\kappa}{\sigma_{11}} \end{aligned} \tag{41}$$

The Bauschinger ratios were calculated using Eq. (41) at 200 °C, 600 °C, 800 °C and 1000 °C, and are presented in Fig. 9. At each temperature level, Bauschinger ratios saw a general decreasing trend except at 1000 °C. The initial plummeting of ϑ_{1000} indicated a drastic shrink of the yield surface. When considering the strain is kept constant, Fig. 9 suggests an increase of Bauschinger ratios from 200 °C to 800 °C followed by a drop as the temperature rises to 1000 °C.

The evolution function parameters of the Bausinchger ratios can be obtained using the least square fitting method, adopting the exponential law as in Eq. (22). The parameters were determined at each temperature level individually as summarised in Table D.2, and subsequently implemented in the Umat subroutine for this verification study. The fitted curves are plotted in Fig. 9 along with the experimental values.

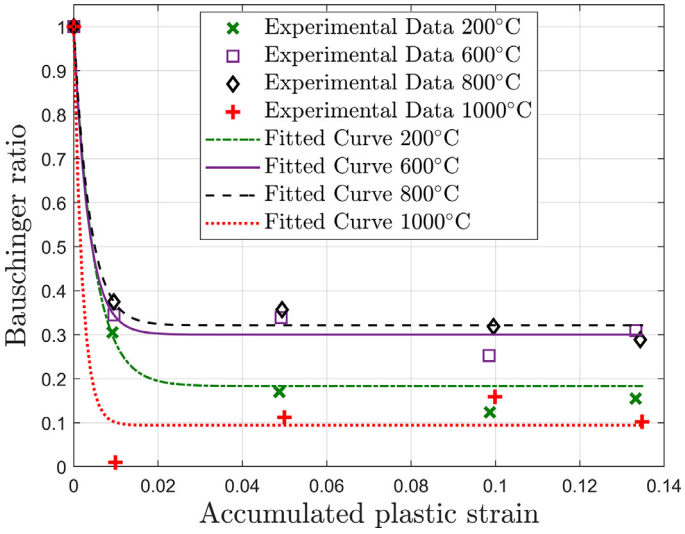

Fig. 9. Bauschinger ratio, least square fitting.

6.2. Finite element model descriptions

The experiments were conducted using specimens of 304L stainless steel rod, following the same reverse yield testing procedures Miller et al. [59] adopted for testing OFHC copper. The specimen is illustrated schematically in Fig. 10.

The cross section of the gauge (outlined in Fig. 10) was modelled using the 4-node plane stress elements in Abaqus/CAE, shown as in Fig. 10. The model was restrained in axial direction on one end. The uniform temperature was applied in the first step. In the second step, a horizontal monotonic tensile load was applied at the other end to a maximum 5.0% axial strain.

The stress strain curves of 304L stainless steel used in the experiments were applied in the material model for the verification. Thus the parameters of the hardening function were obtained by least square fitting the stress strain curves following the same approach adopted for EC 3 carbon steel in Section 4.1.3, and are summarised in Table D.2. The Young's modulus were applied following the reported values : 195.3GPa (20 °C), 182.8GPa (200 °C), 153.8GPa (600 °C), 125.7GPa (800 °C), and 94.3GPa (1000 °C).

6.3. Results and discussions

6.3.1. Comparison study

In the proposed material model, the isotropic hardening variable is computed following Eq. (42).

$$\kappa = \vartheta_T Y_T(\overline{\varepsilon^p}) \tag{42}$$

where Y_T is the isotropic hardening function and $\overline{\varepsilon^p}$ is the accumulated plastic strain.

The kinematic hardening variable in uniaxial stress state, $\overline{\beta}_{11}$, is calculated from Eq. (43) as follows:

$$\overline{\beta}_{11} = \sqrt{\frac{3}{2}}\|\boldsymbol{\beta}\| \tag{43}$$

where $\boldsymbol{\beta}$ is the total backstresses.

The Abaqus results for isotropic hardening (κ) and kinematic hardening ($\overline{\beta}_{11}$) are presented and compared with the experimental data in Fig. 11a and b, respectively. A generally good agreement is observed. The comparison has demonstrated that the evolution of Bauschinger ratio has been successfully implemented in the proposed material model as a function of temperature and accumulated plastic strain.

7. Verification of Bauschinger effect and transient hardening during reverse loading

The Bauschinger effect and the transient hardening behaviour typically observed during reverse loading at room temperature also occur at elevated temperatures.

In this section, the capability of the proposed material model to capture the Bauschinger effect and the transient hardening behaviour is verified using the experimental data obtained by Maciejewski et al. [16], who conducted a series of monotonic and cyclic loading tests on low carbon steel material (A572 Grade Low Carbon) at high temperatures. For the verification purpose, the experimental data of the reversed stress strain relationship of the very first loading loop associated with the monotonic stress strain curve has been used thereby the cyclic hardening/softening effect was excluded.

The testing was performed on cylindrical specimens with an overall length of 114 mm, a gauge length of 25 mm, and a gauge diameter of 11 mm. The same finite element modelling approach as in the previous

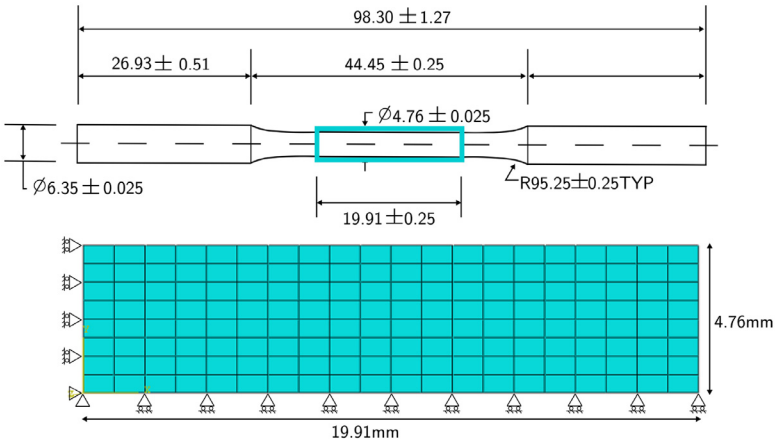

Fig. 10. Reverse yield test specimen (all dimensions in mm) [59].

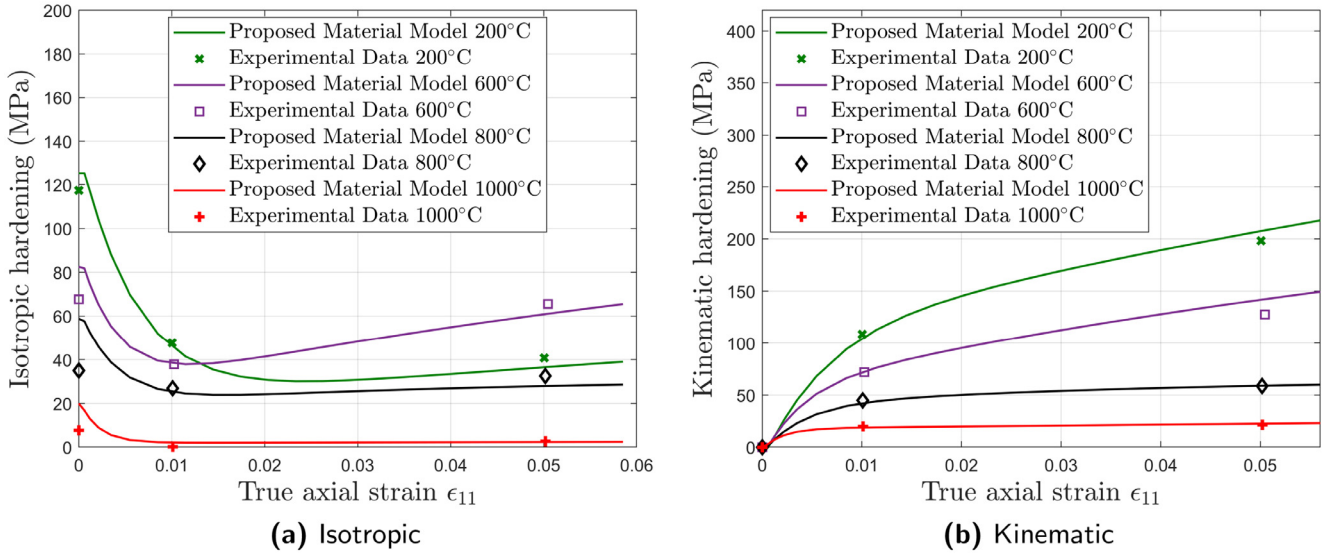

(a) Isotropic **(b)** Kinematic

Fig. 11. Hardening variables comparison.

verification was adopted. The proposed material model was employed for the tested low carbon steel material. The hardening function parameters were obtained by least square fitting the experimental stress strain curves at 300 °C and 700 °C. The material properties of the Young's modulus and the initial yield stress were also calibrated from the experimental data.

The stress strain curve (in red) at 300 °C and 700 °C obtained using least square fitting is compared with the experimental data (blue circle) in Fig. 12a and b respectively. The good agreement observed demonstrated the Voce hardening law successfully captured the nonlinear stress strain relationships of the tested low carbon steel materials at elevated temperatures.

The hardening function parameters obtained, as summarised in Table D.3, were subsequently implemented in the Abaqus Umat code. Three reverse loading tests with varying prestrain levels were simulated in Abaqus to examine the hardening behaviour during reverse loading at 300 °C and 700 °C respectively. The Abaqus stress strain relationship results of monotonic loading range are compared with the curve fitting stress strain curves in Fig. 12a and b, the good agreement suggests the hardening functions have been successfully implemented in Umat.

Varying degrees of transient hardening were predicted by the proposed material model at different prestrain levels. The Bauschinger effect and the transient hardening predicted by the proposed material at the prestrain level experienced in the experiments has been investigated for the verification in the following.

The Bauschinger ratio (ϑ) was determined using Eq. (44), based on the experimental data of the reversed stress strain curves of the very first loading loop at 300 °C and 700 °C, shown in Fig. 13a and b respectively. The S11L is the highest stress point during monotonic loading, and S11U is the lowest stress point before the material yields upon reverse loading, which is the transitional point form the solid blue line to the dashed blue line in the two Figures. The solid blue line presents the loading-unloading range of the stress strain development while the dashed blue line starts from the re-yielding point during reverse loading.

$$\kappa_{11} = \frac{S11L - S11U}{2}; \qquad \alpha_{11} = \frac{S11L + S11U}{2}; \qquad \vartheta = \frac{\kappa_{11}}{\kappa_{11} + \alpha_{11}} \tag{44}$$

where κ_{11} and α_{11} represents the amount of isotropic and the amount of kinematic hardening respectively.

The Bauschinger ratio was therefore 0.790 at 300 °C and 0.724 at 700 °C. The Eq. (22) was adopted in least square fitting to describe the Bauschinger ratio evolution, assuming it would achieve stabilisation shortly after the first strain reversal. The determined evolution function parameters are summarised in Table D.3. The value of b_T in Eq. (22) was

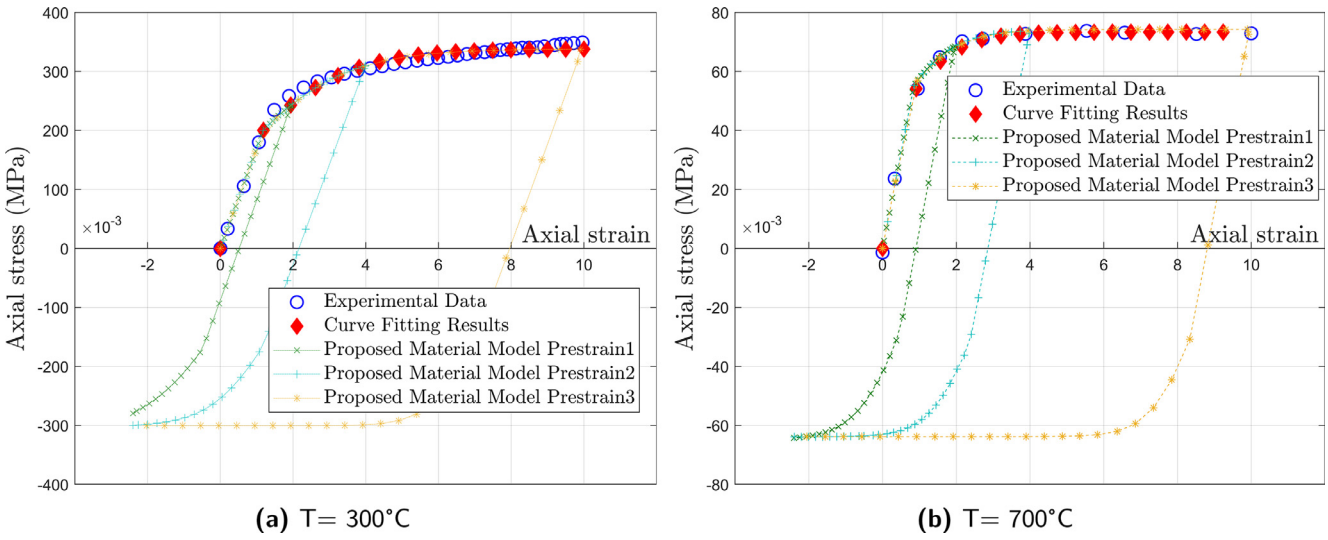

Fig. 12. Stress strain curves comparison.

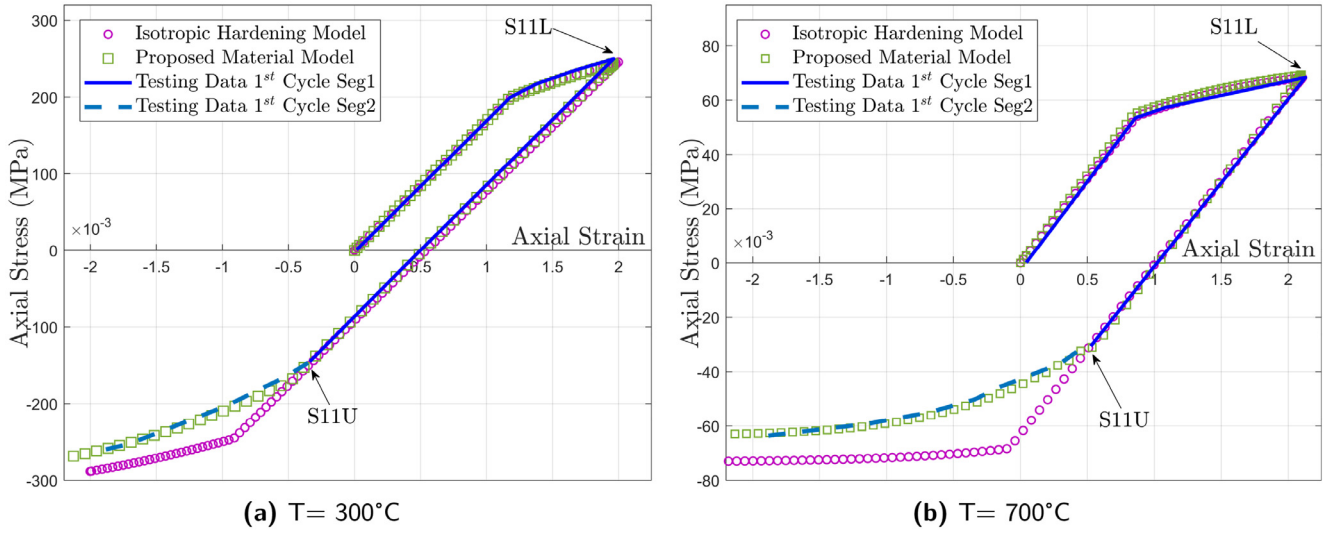

Fig. 13. Hardening models comparison.

adopted for the reverse loading ratio evolution function — Eq. (32), as discussed in Section 5.2.2.

Fig. 13a and b compares the stress strain development during the loading-unloading-reverse loading predicted using isotropic hardening model and the proposed material model with the experimental data at 300° and 700 °C respectively. The proposed material model predicted the re-yielding point very well, properly captured the Bauschinger effect. Beyond the yielding point, the proposed material model also predicted the material's transient hardening behaviour to a degree of satisfactory at both 300 °C and 700 °C.

8. Verification of thermal unloading algorithm

This section focuses on validating the implementation of the algorithm for the re-positioning of the yield surface due to changing temperatures in the Abaqus Umat code. At the thermal step, the new size of the yield surface is determined by Eq. (25) and the new position of the yield surface centre is computed using Eq. (27). The new position of the yield surface induces a reduction in the stress state, a phenomenon commonly referred to as thermal unloading. While the re-positioning of yield surfaces is an invisible internal process, the thermal unloading manifests itself in the changing of mechanical stress, hence can be examined numerically. The verification was therefore performed by comparing the thermal unloading result predicted by the proposed material model to its analytical solution.

The model geometry and the material properties of the low carbon steel at elevated temperatures from previous verification were utilised. A loading scenario has been designed specifically in the following way to accommodate a clear examination of the mechanical behaviour resulted from the re-positioning of the yield surface at the thermal step:

1. Prestrain the material to a mechanical strain level of 0.002, into the plastic region at 300 °C
2. Increase temperature to 700 °C while keeping mechanical strain constant. In this manner any changes in the stress observed at the end of the thermo-mechanical analysis is a result of the yield surface

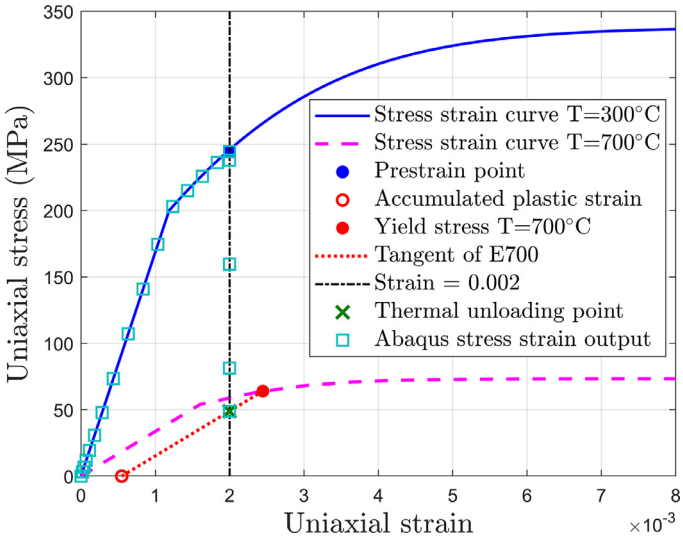

Fig. 14. Thermal unloading verification.

re-positioning due to temperature changes. This is achieved by applying displacement controlled boundary conditions.

Fig. 14 shows the stress strain path during the designed loading process. The prestrain at 300 °C produced an accumulated plastic strain of 5.481×10^{-4}. At 700 °C, the new yield stress = 64.05 MPa (red point) is determined by Eq. (25). For the mechanical strain = 0.002, since $0.002 \times E_{700} < 64.05$, the stress state (0.002,48.91) (green cross) now sits within the yield surface. E_{700} is the elastic modulus at 700 °C. The unloading stress strain development predicted by the proposed material model is shown in blue square, and the final stress state = (0.002,48.89) is computed by the algorithm developed based on Eq. (35). As the thermal unloading behaviour has been successfully captured, it is believed that the algorithm for the re-positioning of the yield surface due to changing temperatures has been correctly implemented in the Umat code.

9. Verification of proposed model in multi-axial loading

In the previous three verifications, the models were subjected to uniaxial loading only. In this section, the proposed material model is further tested under multi-axial loading conditions.

9.1. Experiments in literature review

Lissenden et al. [12] carried out experiments to determine the initial yield surface of 316 stainless steel at room temperature and its subsequent yield surface at elevated temperature 650 °C, with the impact of preloading on the subsequent yield surface also investigated. The experimental data obtained in [12] were employed for this verification.

Tubular specimens fabricated from AISI type 316 stainless steel were used to determine the yield surfaces in the axial (σ_{11})/shear (σ_{12}) stress space. A brief description of the loading procedure and the findings of the experiments is provided in the following sections.

9.1.1. Room temperature

The testing results suggested the initial yield surface could be represented using a circle of radius 82 MPa predicted by the von Mises yield criterion in the modified stress space, with the centre located at (−8 MPa, −4 Mpa) rather than at the origin, possibly due to initial residual stresses.

The impact of prestress on the subsequent yield surfaces was investigated by applying a radial preloading, defined by $\sigma_{12} = \sigma_{11}/\sqrt{3}$, until 50% beyond the initial yield to a maximum stress point (160 MPa, 84 MPa), followed by subsequent unloading to half of the maximum stress level. The subsequent yield surface determined after prestressing showed the distortion typically found for radial preloading which consists mainly of contraction of the yield surface in the preloading direction with a particular flattening on the side nearest origin [60].

9.1.2. Elevated temperature 650 °C

The experiments found that the initial yield surface at 650 °C was a von Mises circle in the modified stress space ($\sigma_{12} = \sigma_{11}/\sqrt{3}$) of a radius of 54 MPa, with its centre located at (−4 MPa, −2 MPa).

Preloading was applied as pure torsion in the elevated temperature case. Maximum tensorial shear strain of 2500 με was applied, followed by subsequent unloading. Three subsequent yield surface determination tests were made for the specimen 316SS22 and 316SS16 respectively, showing translation and elongation in the direction of the preloading (positive torsion).

9.2. Verification model in Abaqus

9.2.1. Model descriptions

The model geometry of Abaqus benchmark example 3.2.1 [61] — a uniformly loaded, elastic-plastic plate, was utilised in this verification study. Since the main objective was to verify the proposed material model algorithm implemented in the Abaqus Umat subroutine, instead of constructing the entire tubular specimen, a simple plate model was used. It allows for a clear assessment of the accuracy of the plasticity model, provided the same loading effect from the experiments can be reproduced in the finite element model.

The key aspect of the chosen loading process in the experiments — axial loading in combination with torsion was to ensure the applied axial stress and shear stress were decoupled. The same loading effect was realised in the Abaqus plate model by applying carefully designed boundary conditions as illustrated in Fig. 15. The boundary conditions were constructed to ensure pure shear force and pure axial force applied in a decoupled manner to the plate of examination, outlined in red. Kinematic coupling was adopted for the nodal constraints.

9.2.2. Material properties

Initial yield stress of the 316SS material at room temperature (147 MPa) and at 650 °C (94 MPa) were calibrated from the experimental results. The elastic modulus is approximately 194.25 GPa at room temperature, and 106.0 GPa at 650 °C. The hardening parameters of the material were determined using the experimental stress strain relationship results as summarised in Table D.4. The Bauschinger ratio was calculated using the maximum positive stress point and negative stress point in the preloading direction of the yield surface results. The parameters of the Bauschinger ratio evolution function are presented in Table D.4.

9.3. Verification results

9.3.1. Initial yield surfaces

Fig. 16a compares the initial yield surfaces of 316SS at room temperature determined by the experimental results and predicted by the proposed material model. The predicted yield surface is an ideal circle in the modified stress space as von Mises yield function is adopted. The experimental data suggests the initial yield surface of 316SS is close to a circle with a degree of anisotropy in compressive yield strength.

At elevated temperature 650 °C, the yield surface determined by the experiments is closer to a von Mises circle than it was at room temperature. The comparison between experimental results and prediction is shown in Fig. 16b.

9.3.2. Subsequent yield surfaces after radial preloading at room temperature

Fig. 17a compares the subsequent yield surface of 316SS after radial prestressing, determined by the experiments and the proposed material

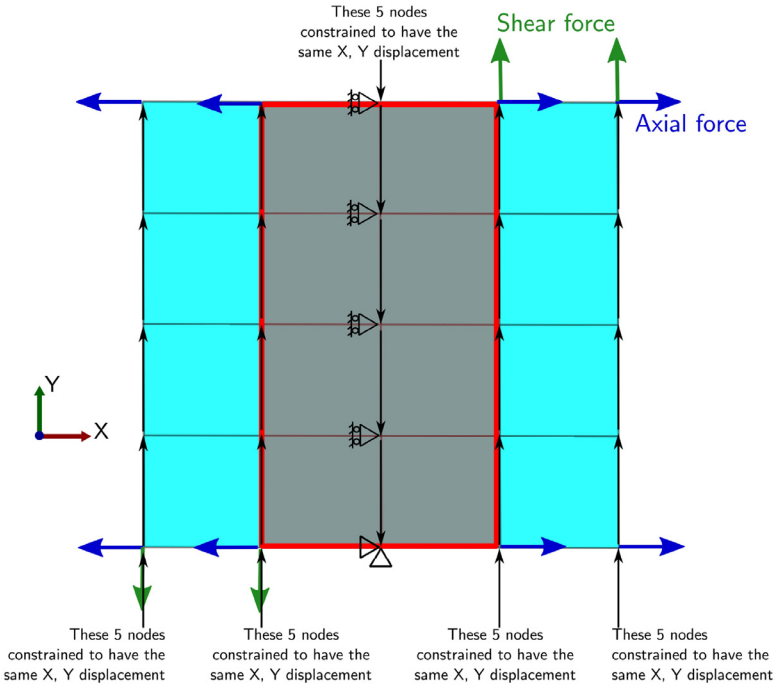

Fig. 15. Abaqus plate model.

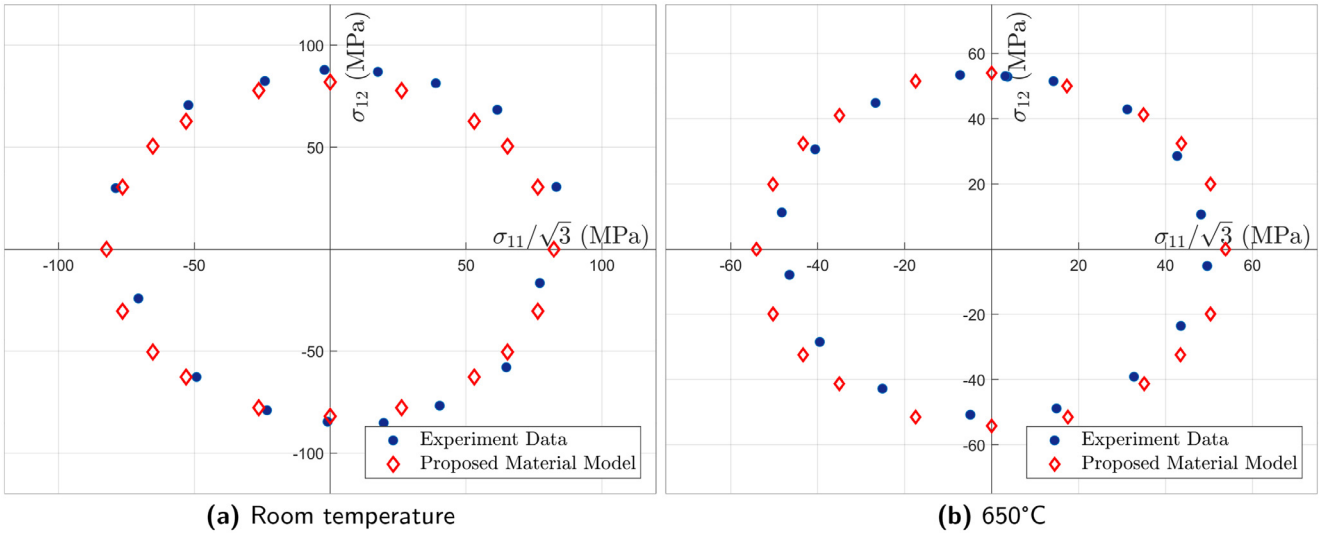

Fig. 16. Initial yield surfaces comparison.

model. The prediction of the proposed material model is an ideal von Mises circle being translated and expanded in the direction of the preloading. The distortion of the subsequent yield surface due to radial preloading was not included. Nevertheless, the translation and expansion of the subsequent yield surface in the direction of the preloading has been clearly captured by the proposed material model.

9.3.3. Subsequent yield surfaces after pure torsion preloading at 650 °C

At the elevated temperature, preloading was applied as pure torsion resulting in no noticeable distortion of the subsequent yield surface, as shown in Fig. 17b. Consequently, the experimental results suggest the subsequent yield surface is an nearly ideal von Mises circle with slight anisotropy in compressive yield strength.

A good agreement has been observed between the experimental results and the predictions. The translation and elongation of the subsequent yield surface in the direction of preloading has been successfully captured by the proposed material model.

10. Application of proposed material model

The implemented material model in Abaqus Umat subroutine [58] was utilised to investigate a single structural steel beam subjected to the complex thermal loading of a 'travelling fire'. Various travelling fire models [3–5,62,63] have been proposed to describe the moving and spreading behaviour of a fire commonly observed in a large open compartment space, which is one of the prominent features of modern architectural design, where the Standard Fire Curve [64] ceased to be applicable. The thermal loading adopted in the study was obtained using the extended travelling fire methodology (ETFM) framework [5]. It is able to capture the realistic thermal loading, e.g.

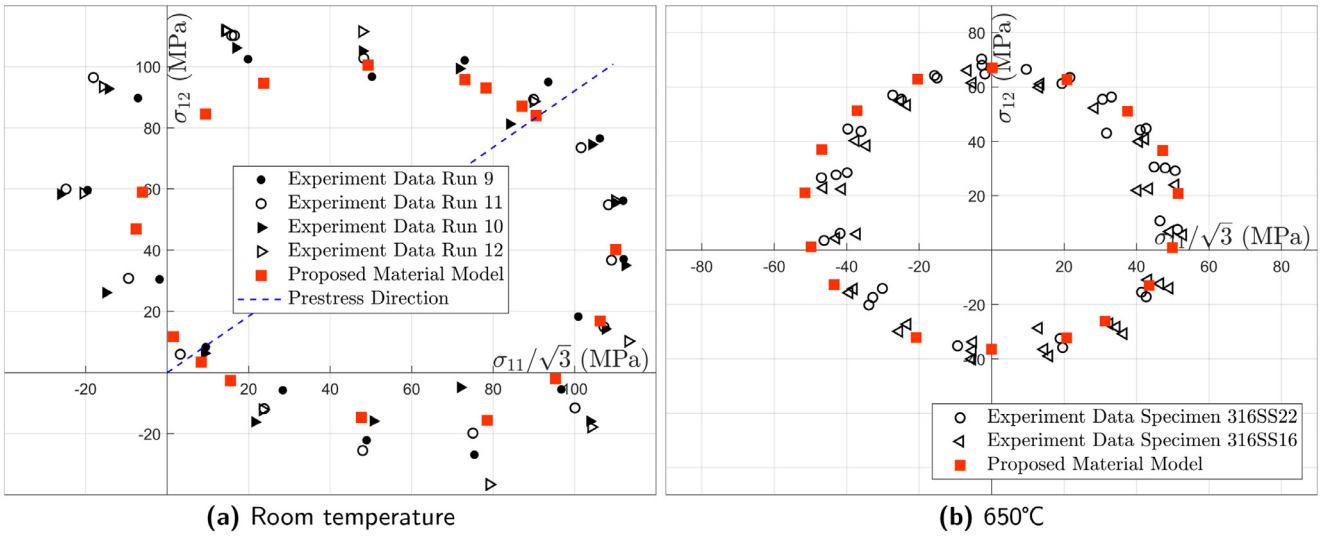

(a) Room temperature **(b)** 650°C

Fig. 17. Subsequent yield surfaces comparison.

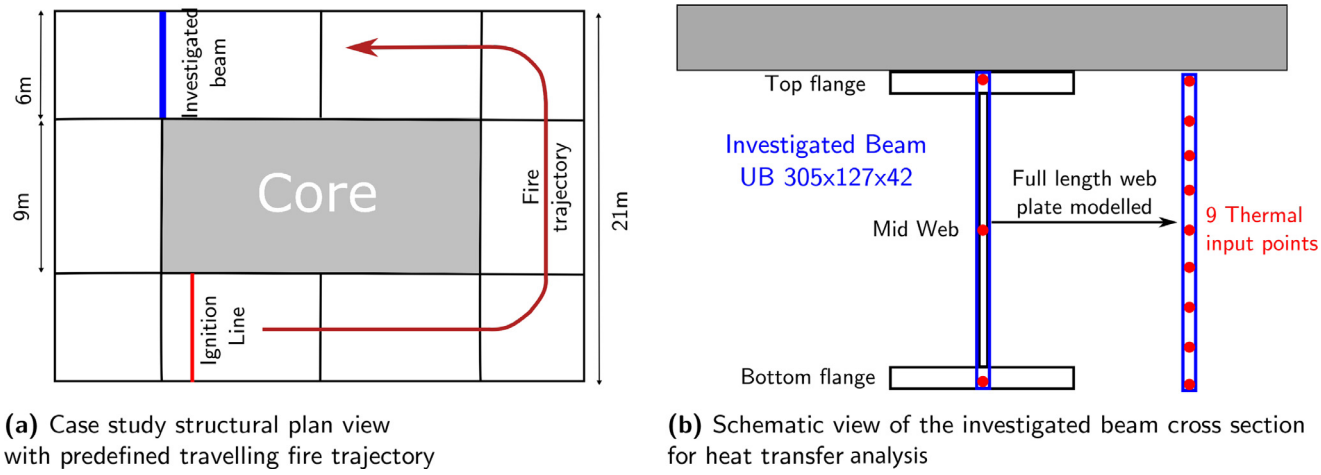

(a) Case study structural plan view with predefined travelling fire trajectory

(b) Schematic view of the investigated beam cross section for heat transfer analysis

Fig. 18. Structural model geometries.

cross-sectional temperature gradient reversal, and 'cyclic' heating and cooling.

The single steel beam (UB 305x127x42) investigated in this case study is located in an idealised structural layout, seen as in Fig. 18a, representing a generic modern tall building with a central core of 162 m^2.

A series of parametric studies were conducted by Dai et al. [6] to investigate the temperature development within the cross section of the beam subjected to travelling fire following the defined trajectory with various combinations of fire spread rate, v (mm/s) and the characteristic fuel load density, $q_{f,k}(MJ/m^2)$. Fig. 19a presents the temperature development of a slow but dense fire (v = 1.6 mm/s; $q_{f,k}$ = 780 MJ/m^2). A nearly uniform temperature development is observed across the cross section and the maximum temperature reached was about 700 °C. Contrastingly, Fig. 19b shows the temperature development of a rapid but light fire (v = 10.0 mm/s; $q_{f,k}$ = 100 MJ/m^2). A more complex cross sectional temperature distribution history was observed. Different cooling rates were experienced at the bottom, centre and top of the cross section, giving rise to the thermal gradient reversal phenomenon — the change of sign of the thermal gradient ratio. The thermal gradient ratio was computed as the temperature ratio between the mid-web and the bottom flange, and between the mid-web and the top flange respectively. A lower maximum temperature of 580 °C was reached in this case.

The complex thermal loading of the rapid light fire was selected in this study in order to best demonstrate the capability of the proposed material model. The temperature history results suggest the thermal gradients only observed along the depth of the web of the I section whereas the temperature development across the thickness of the flanges were uniform because they are thermally thin. Thus the complex thermal loading only occurred within the web plate. A schematic view of the cross-section model of the investigated beam used for heat transfer analysis in [6] is shown in Fig. 18b. For best understanding the structural implications of a complex thermal loading encompassing varying stages of heating and cooling; cross sectional thermal gradient as well as reverse thermal gradient, the study hence focused on examining the structural behaviour of the web plate in particular.

A finite element model of the web plate was built in Abaqus/CAE, as illustrated in Fig. 20. The web plate modelled is 6000 mm long and 306 mm high. The element type of plane stress was assigned to all elements. Both ends of the plate are translationally and rotationally restrained. The EC 3 [20] stress strain curves of carbon steel at elevated

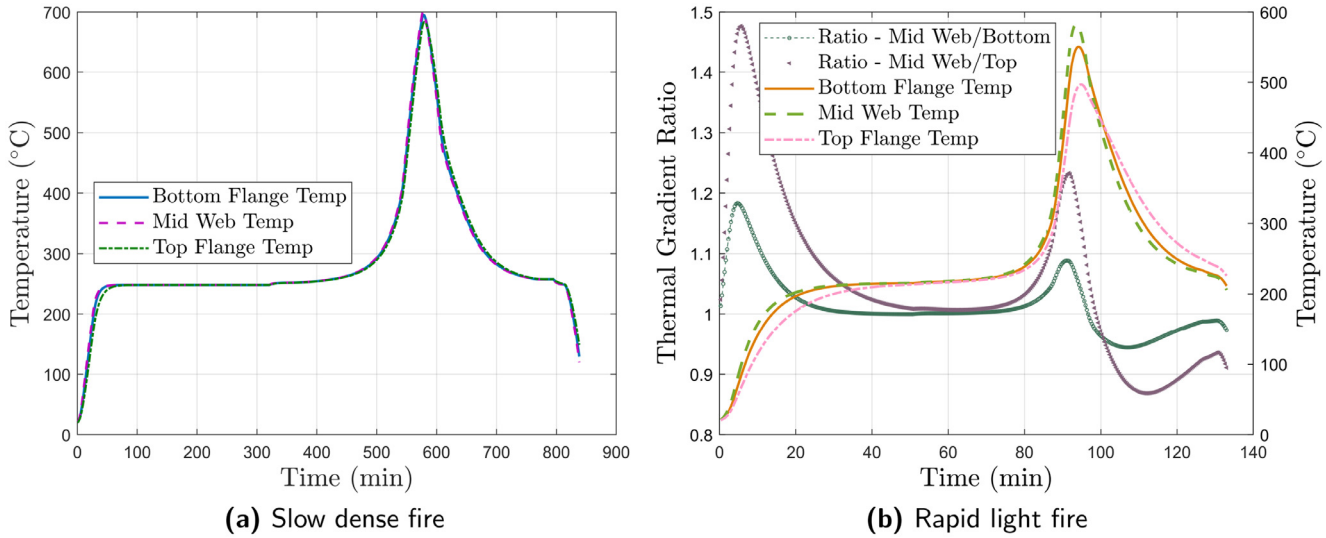

Fig. 19. Temperature history.

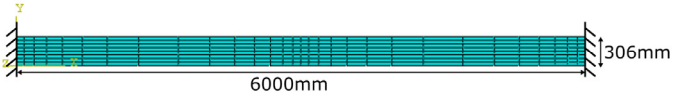

Fig. 20. Single steel beam modelled.

temperatures were adopted. The temperature dependent thermal expansion coefficients (α) have also been defined in accordance with EC 3 [20]. The Bauschinger ratio evolution function determined for the carbon steel material in the verification in Section 7 has been applied for this study.

10.1. Stress/deformation analysis

The thermal loading was applied at 9 points along the depth of the web plate, seen as in Fig. 18b. An initial vertical displacement of 24 mm ($L/250$) was adopted to accommodate the investigation of the influence of initial plastic strain at the onset of a fire.

The development of the midspan deflection and the accumulated plastic strain ($\overline{\varepsilon^p}$) at the bottom of the midspan cross section throughout the fire are presented in Fig. 21a. An earlier stiffness reduction due to initial plastic deformation is indicated by the notable deflection increase observed at around 50 °C, significantly lower than the initiation temperature (100 °C) of steel material's Young's modulus reduction. The change in the tangent of the temperature deflection relationship observed around 220 °C is believed to be caused by the change of thermal gradient occurred in the temperature history, as seen in Fig. 19b. At around 500 °C the curvature of the temperature deflection curve started to change quickly, indicating substantial beam stiffness reduction as a result of material degradation. During the cooling stage, the deflection experienced a recovery as the steel material regained its stiffness. The development of the $\overline{\varepsilon^p}$ correlated to that of the deflection during the heating stage. While during cooling, the $\overline{\varepsilon^p}$ still experienced growth due to continuous stress development.

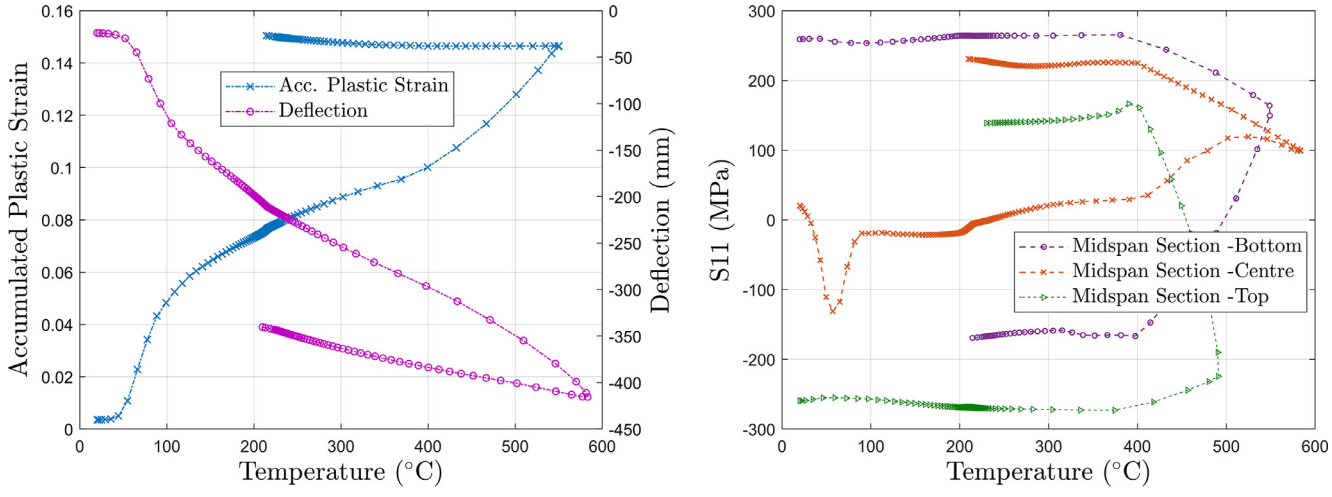

Fig. 21. Stress/Deformation analysis results.

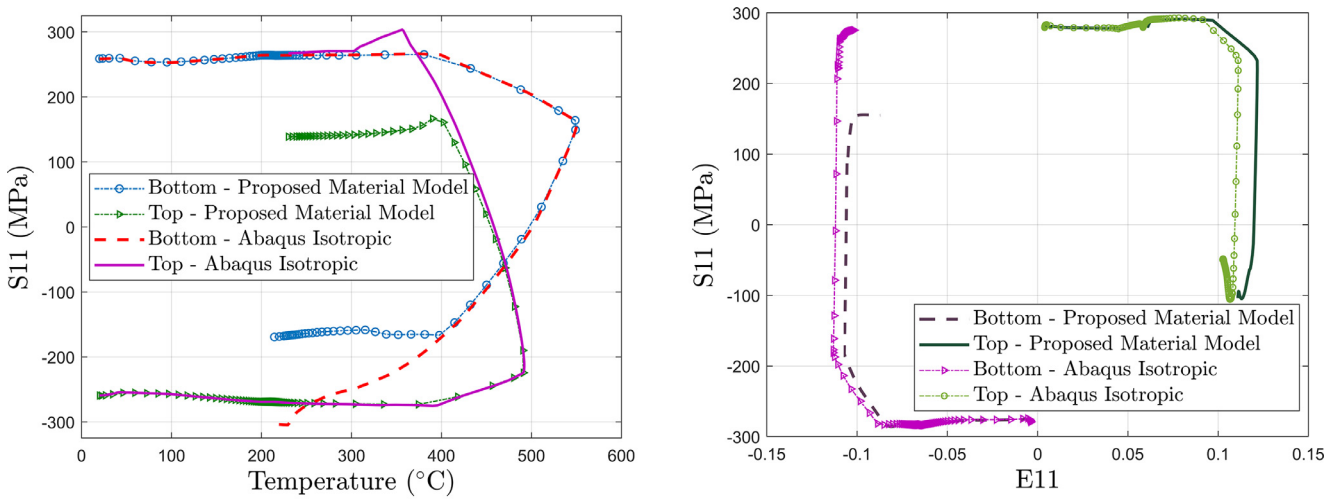

(a) Midspan S11 development **(b)** End span axial stress (S11) — axial strain (E11)

Fig. 22. Proposed material model v.s. Isotropic hardening model.

The development of axial stress (S11) at midspan cross section is plotted in Fig. 21b. At the start of the fire, the section is in sagging bending moment — S11 is positive at the bottom, nearly zero at the centre and negative at the top. As temperature rises, compressive stress starts to develop due to restrained thermal expansion, giving rise to an evident negative growth of S11 as observed at the centre of the cross section. At around 70 °C, the centre S11 sees a shift to tension, because the P-Delta effect of the thermal expansion induced compression. It is interesting to note that the development of the centre S11 suggests the whole cross section did not reach plastic state until much later in the cooling stage.

The evolution of S11 at the bottom and the top of the cross section exhibited different behaviour from that at the centre since they had already been in the plastic state before the fire. They started to decrease at about 400 °C due to the reduction in the yielding value of the material.

The structure behaved as expected under the thermal loading, the plastic deformation due to heating and cooling has been successfully captured by the proposed material model.

10.2. Comparison study

A comparison study of the structural response of the beam using the proposed material model and the isotropic hardening model in Abaqus was performed. Fig. 22a compares the stress development during the fire at the top and the bottom of the midspan cross section produced using the two material models respectively. Identical monotonic stress increase and evident stress reversals were observed. The key difference was the yielding during the reverse, where a lower yield stress was observed in the results of the proposed material model due to the Bauschinger effect.

The comparison of the stress strain curve at the end span cross section is presented Fig. 22b. The Bauschinger effect and the transient hardening behaviour have been clearly captured by the proposed material model.

11. Summary and conclusions

In this paper, a new combined isotropic-kinematic hardening model has been developed for assessing steel materials for thermo-mechanical analysis with fire.

Harley et al. [15] observed substantial development of $\bar{\beta}_{11}$ and swift drop of κ within the first 1.0% of straining at elevated temperatures in 304L stainless steel. Different steel materials will exhibit different degrees of Bauschinger effects [65]. Due to limited available testing data on the evolution of isotropic hardening and kinematic hardening variables at elevated temperatures, it was not possible to carry out more verifications than those presented.

However, it should be noted that the verification was conducted to demonstrate the capability of the proposed material model to capture the temperature dependent Bauschinger effects, not to justify for any particular materials. Thus different sets of temperature dependent function parameters should be adopted for different materials accordingly. The effect of varying function parameters on the stability of the proposed model is not investigated herein due to limited available testing data. A sensitivity study dedicated to this subject is of great interests for the further development of the model.

By adopting two non-linear kinematic hardening variables, the proposed material model is capable of modelling the Bauschinger effect and transient hardening behaviour at elevated temperatures efficiently.

Due to the lack of experimental data on the re-positioning of yield surface centre at elevated temperatures, the corresponding algorithms was verified by comparing the thermal unloading stress result of the proposed material model to its analytical solution.

The multi-axial verification results demonstrated that the proposed material model has been successfully implemented for three dimensional stress analysis. It is capable of capturing the expansion and the translation of yield surfaces, presenting the yield surface as a von Mises circle.

In conclusion, the capability of the proposed material model for capturing the Bauschinger effect and transient hardening behaviour at elevated temperatures has been demonstrated. The proposed model has been successfully implemented in the Abaqus Umat subroutine and was utilised to analyse the structural behaviour of a single beam structure under complex realistic building fires.

Appendix A. Numerical algorithm for proposed combined isotropic and kinematic hardening model

The numerical algorithm of the proposed combined isotropic and kinematic hardening model for thermo-mechanical analysis of structures in fire described in the preceding section is summarised in Table A.1. The proposed model is implemented into the commercial finite element code Abaqus/Standard, using the user subroutine — Umat [58].

Table A.1
Numerical algorithm for the proposed combined isotropic and kinematic hardening model.

Last Converged Step n
If Temperature change $\Delta T \neq 0$, Go to Thermal Step, Else Go to Mechanical Step

Thermal Step, Current Temperature T_{n+1},
1. Update Temperature dependent Parameters
Young's modulus E_{Tn+1}, Initial yield stress $\sigma_{p,Tn+1}$
Hardening function parameters v_{Tn+1} and δ_{Tn+1}
Bauschinger ratio evolution equation parameters a_{Tn+1}, b_{Tn+1} and c_{Tn+1}
Material model parameter Vh_{Tn+1}
2. Update Bauschinger ratio
$\vartheta_{Tn+1} = a_{Tn+1} * exp(-b_{Tn+1} * \overline{\varepsilon^p}_n) + c_{Tn+1}$
3. Update the size of bounding surface
$Y = \sqrt{\frac{2}{3}} Y_{1D,Tn+1}(\overline{\varepsilon^p_n})$
4. Update the position of the yield surface centre, $\boldsymbol{\beta_1}$ term
$\boldsymbol{\beta_1}_n = (1.0 - \vartheta_{Tn+1}) Y \frac{\boldsymbol{\varepsilon}^p_n}{\|\boldsymbol{\varepsilon}^p_n\|}$
Mechanical Step, Strain Increment $\Delta\boldsymbol{\varepsilon}$
1. Elastic predictor
$\boldsymbol{\sigma}^{trial}_{n+1} = \boldsymbol{C}_{n+1} \cdot (\boldsymbol{\varepsilon}_n + \Delta\boldsymbol{\varepsilon} - \boldsymbol{\varepsilon}^p{}_n)$, $\boldsymbol{\beta_1}^{trial}_{n+1} = \boldsymbol{\beta_1}_n$, $\boldsymbol{\beta_2}^{trial}_{n+1} = \boldsymbol{\beta_2}_n$
$\boldsymbol{s}^{trial}_{n+1} = \boldsymbol{I_{dev}} : \boldsymbol{\sigma}^{trial}_{n+1}$, $\boldsymbol{I_{dev}} = \boldsymbol{I} - \frac{1}{3}\mathbf{1} \otimes \mathbf{1}$
$\boldsymbol{\eta}^{trial}_{n+1} = \boldsymbol{s}^{trial}_{n+1} - \boldsymbol{\beta_1}^{trial}_{n+1} - \boldsymbol{\beta_2}^{trial}_{n+1}$, $\boldsymbol{N_{n+1}} = \frac{\boldsymbol{\eta}^{trial}_{n+1}}{\|\boldsymbol{\eta}^{trial}_{n+1}\|}$
$\vartheta_{n+1} = a_{n+1} * exp(-b_{n+1} * \overline{\varepsilon^p}_n) + c_{n+1}$
$v_{n+1} = 1.0 - exp(-b_{n+1} * \overline{\varepsilon^p_l}_n)$
Reverse loading index :$l^{trial}_{n+1} = l_n$
$\overline{\beta_l}^{trial}_{n+1} = \overline{\beta_l}_n$
• Check the reverse loading criterion according to Eq. (30)
If $cos(\theta) < 0.0$ then
$l^{trial}_{n+1} = l_n + 1$
$\overline{\epsilon^p_l}^{trial}_{n+1} = 0.0$
$\overline{\beta_l}^{trial}_{n+1} = Vh_{Tn+1}\sqrt{\frac{3}{2}(\boldsymbol{\beta_1}_n + \boldsymbol{\beta_2}_n) : (\boldsymbol{\beta_1}_n + \boldsymbol{\beta_2}_n)}$
$\boldsymbol{\beta_2}^{trial}_{n+1} = 0.0$
Else, Do nothing
• Check the yield condition
If $f(\boldsymbol{\eta}^{trial}_{n+1}) - \vartheta_{n+1} Y_{1D,n+1}(\overline{\varepsilon^p}) < Tolerance$, then Set $(\bullet)_{n+1} = (\bullet)^{Trial}$ Exit
Else Go to Plastic corrector
2. Plastic corrector
• Newton-Raphson iteration is employed to determine plastic multiplier $\Delta\gamma$. Initialise $\Delta\gamma = 0.0$
Iterate until $|g(\Delta\gamma)| < Tolerance$
$g(\Delta\gamma) = \| \boldsymbol{\eta}^{trial}_{n+1} \| - 2 * \mu_{n+1} * \Delta\gamma - \vartheta_{n+1}\sqrt{\frac{2}{3}} * Y_{1D,n+1}(\overline{\varepsilon^p_n} + \sqrt{\frac{2}{3}}\Delta\gamma)$
$dg(\Delta\gamma) = -2 * \mu_{n+1} - \frac{2}{3} * [Y'_{1D,(n+1)}(\overline{\varepsilon^p_n} + \sqrt{\frac{2}{3}}\Delta\gamma)] * \vartheta_{n+1}$
Y' is the first derivative of Y with regard to $\Delta\gamma$
$\Delta\gamma = \Delta\gamma - g/dg$
∘ ϑ_{n+1} is considered a constant during the Newton-Raphson iteration for small step of $\Delta\gamma$.
The consequent 'residual stress' of this simplification will be solved in the next iteration.
3. Update stress state
$\boldsymbol{\varepsilon}^p{}_{n+1} = \boldsymbol{\varepsilon}^p{}_n + \Delta\gamma \boldsymbol{N}_{n+1}$; $\overline{\varepsilon^p_{n+1}} = \overline{\varepsilon^p_n} + \sqrt{\frac{2}{3}}\Delta\gamma$; $\overline{\varepsilon^p_l}_{(n+1)} = \overline{\varepsilon^p_l}^{trial}_{n+1} + \sqrt{\frac{2}{3}}\Delta\gamma$
$l_{n+1} = l^{trial}_{n+1}$
$\vartheta_n = c + a * exp(-b * \overline{\varepsilon^p_n})$; $\vartheta_{n+1} = c + a * exp(-b * \overline{\varepsilon^p_{n+1}})$
If $l_{n+1} \neq 0$ then
$v_n = 1 - exp(-b * \overline{\varepsilon^p_l}_{(n)})$; $v_{n+1} = 1 - exp(-b * \overline{\varepsilon^p_l}_{(n+1)})$
$\overline{\beta_2} = (v_{n+1} - v_n) * \overline{\beta_l}^{trial}_{n+1}$; $\boldsymbol{\beta_2}_{n+1} = \boldsymbol{\beta_2}^{trial}_{n+1} + \overline{\beta_2}\boldsymbol{N}_{n+1}$
Endif
$\boldsymbol{\beta_1}_{n+1} = \boldsymbol{\beta_1}^{trial}_{n+1} + \sqrt{\frac{2}{3}} * [(1 - \vartheta_{n+1}) Y_{(n+1)}(\overline{\varepsilon^p}_{n+1}) - (1 - \vartheta_n) Y_{(n+1)}(\overline{\varepsilon^p}_n)]\boldsymbol{N}_{n+1}$
$\boldsymbol{\sigma}_{n+1} = \boldsymbol{\sigma}^{trial}_{n+1} - 2 * \mu_{(n+1)} * \Delta\gamma \boldsymbol{N}_{n+1}$

Appendix B. Implementation for plane stress material model

The algorithms developed in Section 5 are based on elastoplastic three-dimensional constitutive equations. To implement the three-dimensional plasticity algorithm to plane stress elements, a global Newton-Raphson iteration loop has been used to enforce the plane stress constraint $\sigma_{33} = 0$ at the Gauss point level, following the approach introduced by Dodds [66].

The overall algorithm implemented is summarised in Table B.1, where D_{22} is the component of the axisymmetric consistent tangent matrix:

$$\begin{bmatrix} d\sigma_{11} \\ d\sigma_{22} \\ d\sigma_{12} \\ \hline d\sigma_{33} \end{bmatrix} = \left[\begin{array}{cc|c} & & \\ \boldsymbol{D_{11}} & & \boldsymbol{D_{12}} \\ & & \\ \hline \boldsymbol{D_{21}} & & D_{22} \end{array}\right] \begin{bmatrix} d\varepsilon^{e\ trial}_{11} \\ d\varepsilon^{e\ trial}_{22} \\ 2d\varepsilon^{e\ trial}_{12} \\ \hline d\varepsilon^{e\ trial}_{33} \end{bmatrix} \tag{B.1}$$

It is noted that for the above methodology a number of iterations will be required in each Gauss point to ensure the plane stress condition. Consequently, the present procedure can be computational expensive. However the cost of the calculations carried out at Gauss point level

Table B.1
Numerical algorithm for plane stress material.

1. Set initial guess for the elastic trial thickness strain to the converged value from last step $\varepsilon_{33}^{e\ trial} = (\varepsilon_{33}^{e})_n$
2. Call the stress integration algorithm in Table A.1
3. For the obtained trial σ_{33}, if $|\sigma_{33}| <$ Tolerance, Then Exit loop
4. Compute component D22 of the consistent tangent matrix
5. Apply Newton-Raphon correction to the thickness trial strain $\varepsilon_{33}^{e\ trial} := \varepsilon_{33}^{e\ trial} - \frac{\sigma_{33}}{D_{22}}$
6. Go to Step 2

increases linearly with the problem size, whereas the cost of the solution of the global linearised problem increases at a much higher nonlinear rate [34].

The elastoplastic consistent tangent modulus obtained in Section 5.4 for three dimensional plasticity was modified for the plane stress plasticity to ensure the tangent operator remain consistent with the above nested iteration algorithm. The elastoplastic consistent tangent modulus is derived by first differentiating the residual equation of the plane stress enforcement loop : $\sigma_{33} = 0$. Together with Eq. (B.1), it gives:

$$\begin{aligned} d\sigma_{33} &= \boldsymbol{D_{21}} d\boldsymbol{\varepsilon}_{n+1}^{e\ trial} + D_{22} d\varepsilon_{33}^{e\ trial} = 0 \\ &\Rightarrow d\varepsilon_{33}^{e\ trial} = \frac{-1}{D_{22}} \boldsymbol{D_{21}} d\boldsymbol{\varepsilon}^{e\ trial} \end{aligned} \tag{B.2}$$

Replacing Eq. (B.2) into Eq. (B.1) results in the following consistent tangent relation between in-plane stress and strain components:

$$\frac{d\boldsymbol{\sigma}_{n+1}}{d\boldsymbol{\varepsilon}_{n+1}^{e\ trial}} = \boldsymbol{D_{11}} - \frac{1}{D_{22}} \boldsymbol{D_{12}} \boldsymbol{D_{21}} \tag{B.3}$$

For the von Mises model, the above Eq. (B.3) relates the elastoplastic consistent tangent modulus to generic three dimensional expression as follows:

$$D_{ijkl}^{ep,PlaneStress} = D_{ijkl}^{ep,3D} - D_{ij33}^{ep,3D} \frac{D_{33kl}^{ep,3D}}{D_{3333}^{ep,3D}} \tag{B.4}$$

The above Eq. (B.4) has been implemented in the Abaqus subroutine Umat [58] for performing plane stress analysis using shell elements.

Appendix C. Derivation of elastoplastic consistent tangent modulus D^{ep}

When the material is subjected to monotonic loading, the yield condition function can be reduced to the Eq. (C.1) below, which then becomes differentiable:

$$\Phi(\Delta\gamma) \equiv \|\boldsymbol{\eta}_{n+1}^{trial}\| - 2\mu\Delta\gamma - (\overline{\beta}_{1n+1} - \overline{\beta}_{1n}) - \sigma_{y,iso} = 0 \tag{C.1}$$

During reverse loading, the elastoplastic consistent tangent modulus shall be derived using the Eq. (C.2):

$$\Phi(\Delta\gamma) \equiv \|\boldsymbol{\eta}_{n+1}^{trial}\| - 2\mu\Delta\gamma - (\overline{\beta}_{1n+1} - \overline{\beta}_{1n}) - (\overline{\beta}_{2n+1} - \overline{\beta}_{2n}) - \sigma_{y,iso} = 0 \tag{C.2}$$

The following section focuses on presenting in details the derivation of the elastoplastic consistent tangent modulus for the proposed material model under monotonic loading case. The derived elastoplastic consistent tangent operator for the reverse loading case will be provided at the end of this section.

Substituting Eq. (25) and 26 into Eq. (C.1) gives:

$$\begin{aligned} \Phi(\Delta\gamma) \equiv \|\boldsymbol{\eta}_{n+1}^{trial}\| - 2\mu\Delta\gamma - (1-\vartheta_n)\left[\sqrt{\frac{2}{3}} Y_{1D}\left(\overline{\varepsilon^p}_n + \sqrt{\frac{2}{3}}\Delta\gamma\right) - \overline{\beta}_n\right] \\ -\vartheta_n \sqrt{\frac{2}{3}} Y_{1D}\left(\overline{\varepsilon^p}_n + \sqrt{\frac{2}{3}}\Delta\gamma\right) = 0 \end{aligned}$$

Re-arranging and combining the terms related to Y_{1D} gives:

$$\Phi(\Delta\gamma) \equiv \|\boldsymbol{\eta}_{n+1}^{trial}\| - 2\mu\Delta\gamma - (1-\vartheta_n)\overline{\beta}_n - \sqrt{\frac{2}{3}} Y_{1D}\left(\overline{\varepsilon^p}_n + \sqrt{\frac{2}{3}}\Delta\gamma\right) = 0 \tag{C.3}$$

where the Bauschinger ratio (ϑ) is considered of constant value of ϑ_n during the Newton-Raphson iteration for increment (n+1).

The m^{th} Newton-Raphson iterative correction to $\Delta\gamma$ for the solution of Eq. (C.3) reads:

$$\Delta\gamma^{(m)} := \Delta\gamma^{(m-1)} - \frac{\Phi(\Delta\gamma^{(m-1)})}{d} \tag{C.4}$$

where

$$d = -2\mu - \frac{2}{3} H_{1D}\left(\overline{\varepsilon^p}_n + \sqrt{\frac{2}{3}}\Delta\gamma\right) \tag{C.5}$$

where $H_{1D} \equiv Y'_{1D}$ is the slope of the uniaxial tensile stress— plastic strain curve.

The incremental algorithmic constitutive update function for $\boldsymbol{\sigma_{n+1}}$ for the von Mises model with nonlinear combined hardening using back-Euler return mapping is:

$$\Delta\boldsymbol{\sigma} = \boldsymbol{D}^e : \Delta\boldsymbol{\varepsilon} - 2\mu\Delta\gamma\boldsymbol{N} \tag{C.6}$$

where $\Delta\boldsymbol{\varepsilon}$ is the deviatoric strain increment, γ is the plastic multiplier, $\boldsymbol{D^e}$ is the constant isotropic elasticity tensor

$$\begin{aligned} \boldsymbol{D}^e &= \kappa \mathbf{1} \otimes \mathbf{1} + 2\mu \boldsymbol{I_{dev}} \\ \boldsymbol{I_{dev}} &= \boldsymbol{I} - \frac{1}{3}\mathbf{1} \otimes \mathbf{1} \end{aligned} \tag{C.7}$$

where κ is the bulk modulus, μ is the shear modulus, $\boldsymbol{I}$ is the fourth-order symmetric unit tensor, and $\mathbf{1}$ is the second-order symmetric unit tensor.

The deviatoric unit flow vector ($\boldsymbol{N}$) is:

$$\boldsymbol{N} = \frac{\boldsymbol{\eta}_{n+1}}{\|\boldsymbol{\eta}_{n+1}\|} = \frac{\boldsymbol{\eta}_{n+1}^{trial}}{\|\boldsymbol{\eta}_{n+1}^{trial}\|} \tag{C.8}$$

Differentiate the stress update Eq. (C.6) gives:

$$\frac{\partial\Delta\boldsymbol{\sigma}}{\partial\Delta\boldsymbol{\varepsilon}} = \boldsymbol{D}^e - 2\mu\boldsymbol{N} \otimes \frac{\partial\Delta\gamma}{\partial\Delta\boldsymbol{\varepsilon}} - 2\mu\Delta\gamma\frac{\partial\boldsymbol{N}}{\partial\Delta\boldsymbol{\varepsilon}} \tag{C.9}$$

The incremental plastic multiplier derivation ($\frac{\partial\Delta\gamma}{\partial\Delta\boldsymbol{\varepsilon}}$) is obtained by differentiating the yield condition Eq. (C.3) with respect to deviatoric trial strain $\boldsymbol{\varepsilon}$

$$\begin{aligned} &\Phi(\boldsymbol{\eta}_{n+1}, \boldsymbol{\varepsilon^p}_{n+1}) = \Phi(\boldsymbol{\eta}_n, \boldsymbol{\varepsilon^p}_n) = 0 \\ &\qquad \Rightarrow \frac{\partial\Phi}{\partial\Delta\boldsymbol{\varepsilon}} = 0 \\ &\frac{\partial\Phi}{\partial\Delta\boldsymbol{\varepsilon}} = \frac{\partial}{\partial\Delta\boldsymbol{\varepsilon}}\left[\|\boldsymbol{\eta}_{n+1}^{trial}\| - 2\mu\Delta\gamma - (1-\vartheta_n)\overline{\beta}_n - \sqrt{\frac{2}{3}} Y_{1D}\left(\overline{\varepsilon^p}_n + \sqrt{\frac{2}{3}}\Delta\gamma\right)\right] = 0 \\ &\qquad \Rightarrow \frac{\partial\|\boldsymbol{\eta}_{n+1}^{trial}\|}{\partial\Delta\boldsymbol{\varepsilon}} - 2\mu\frac{\partial\Delta\gamma}{\partial\Delta\boldsymbol{\varepsilon}} - \frac{2}{3} H_{1D}\left(\overline{\varepsilon^p}_n + \sqrt{\frac{2}{3}}\Delta\gamma\right)\frac{\partial\Delta\gamma}{\partial\Delta\boldsymbol{\varepsilon}} = 0 \end{aligned} \tag{C.10}$$

The derivative of relative stress tenor ($\frac{\partial \boldsymbol{\eta}_{n+1}^{trial}}{\partial \Delta \boldsymbol{\varepsilon}}$) can be obtained by following:

$$\frac{\partial \boldsymbol{\eta}_{n+1}^{trial}}{\partial \Delta \boldsymbol{\varepsilon}} = \frac{\partial (\boldsymbol{s}_{n+1}^{trial} - \boldsymbol{\beta}_n)}{\partial \Delta \boldsymbol{\varepsilon}} = 2\mu \boldsymbol{I}_{\boldsymbol{dev}} \tag{C.11}$$

Subsequently we have:

$$\begin{aligned} \|\boldsymbol{\eta}_{n+1}^{trial}\| &= \left(\boldsymbol{\eta}_{n+1}^{trial} : \boldsymbol{\eta}_{n+1}^{trial}\right)^{1/2} \\ \Rightarrow \frac{\partial \|\boldsymbol{\eta}_{n+1}^{trial}\|}{\partial \Delta \boldsymbol{\varepsilon}} &= \frac{1}{2}\left(\boldsymbol{\eta}_{n+1}^{trial} : \boldsymbol{\eta}_{n+1}^{trial}\right)^{-1/2} 2\boldsymbol{\eta}_{n+1}^{trial} : \frac{\partial \boldsymbol{\eta}_{n+1}^{trial}}{\partial \Delta \boldsymbol{\varepsilon}} \\ &= \frac{\boldsymbol{\eta}_{n+1}^{trial}}{\|\boldsymbol{\eta}_{n+1}\|} : 2\mu \boldsymbol{I}_{\boldsymbol{dev}} = 2\mu \boldsymbol{N} \end{aligned} \tag{C.12}$$

After substitution of Eq. (C.12) into Eq. (C.10) we can therefore obtain $\frac{\partial \boldsymbol{\eta}_{n+1}^{trial}}{\partial \Delta \boldsymbol{\varepsilon}}$:

$$2\mu \boldsymbol{N} - \left(2\mu + \frac{2}{3} H_{1D}\left(\overline{\varepsilon^p}_n + \sqrt{\frac{2}{3}}\Delta\gamma\right)\right)\frac{\partial \Delta\gamma}{\partial \Delta \boldsymbol{\varepsilon}} = 0$$

$$\Rightarrow \frac{\partial \Delta\gamma}{\partial \Delta \boldsymbol{\varepsilon}} = 2\mu \boldsymbol{N}\Theta$$

$$\Theta = 2\mu + \frac{2}{3} H_{1D}\left(\overline{\varepsilon^p}_n + \sqrt{\frac{2}{3}}\Delta\gamma\right) \tag{C.13}$$

The derivative of the deviatoric unit flow vector ($\frac{\partial \boldsymbol{N}}{\partial \Delta \boldsymbol{\varepsilon}}$) is obtained as follows:

$$\frac{\partial \boldsymbol{N}}{\partial \Delta \boldsymbol{\varepsilon}} = \frac{\partial \boldsymbol{N}}{\partial \Delta \boldsymbol{\eta}_{n+1}^{trial}} : \frac{\partial \boldsymbol{\eta}_{n+1}^{trial}}{\partial \Delta \boldsymbol{\varepsilon}} \tag{C.14}$$

We have

$$\begin{aligned} \frac{\partial \boldsymbol{N}}{\partial \Delta \boldsymbol{\eta}_{n+1}^{trial}} &= \frac{\partial}{\partial \boldsymbol{\eta}_{n+1}^{trial}}\left(\frac{\boldsymbol{\eta}_{n+1}^{trial}}{\|\boldsymbol{\eta}_{n+1}^{trial}\|}\right) = \frac{\boldsymbol{I}}{\|\boldsymbol{\eta}_{n+1}^{trial}\|} - \frac{\boldsymbol{\eta}_{n+1}^{trial} \otimes \boldsymbol{\eta}_{n+1}^{trial}}{\|\boldsymbol{\eta}_{n+1}^{trial}\|^3} \\ &= \frac{1}{\|\boldsymbol{\eta}_{n+1}^{trial}\|}[\boldsymbol{I} - \boldsymbol{N} \otimes \boldsymbol{N}] \end{aligned} \tag{C.15}$$

Substituting Eq. (C.15) and C.11 into Eq. (C.14) gives:

$$\frac{\partial \boldsymbol{N}}{\partial \Delta \boldsymbol{\varepsilon}} = \frac{1}{\|\boldsymbol{\eta}_{n+1}^{trial}\|}[\boldsymbol{I} - \boldsymbol{N} \otimes \boldsymbol{N}] : 2\mu \boldsymbol{I}_{\boldsymbol{dev}} = \frac{2\mu}{\|\boldsymbol{\eta}_{n+1}^{trial}\|}[\boldsymbol{I}_{\boldsymbol{dev}} - \boldsymbol{N} \otimes \boldsymbol{N}] \tag{C.16}$$

Finally, substituting Eq. (C.13) and C.16 into Eq. (C.9), the elastoplastic consistent tangent can be obtained:

$$\boldsymbol{D}^{ep} = \boldsymbol{D}^{e} - 4\mu^2 \Theta \boldsymbol{N} \otimes \boldsymbol{N} - \frac{4\mu^2}{\|\boldsymbol{\eta}_{n+1}^{trial}\|}[\boldsymbol{I}_{\boldsymbol{dev}} - \boldsymbol{N} \otimes \boldsymbol{N}] \tag{C.17}$$

During reverse loading, the elastoplastic consistent tangent can still be computed following Eq. (C.17), with the term Θ modified to include the $\boldsymbol{\beta_2}$ term as follows:

$$\Theta = 2\mu + \frac{2}{3} H_{1D}\left(\overline{\varepsilon^p}_n + \sqrt{\frac{2}{3}}\Delta\gamma\right) - \frac{2}{3}\overline{\beta}_l \exp\left(-b\left(\overline{\varepsilon^p}_{l\,n} + \sqrt{\frac{2}{3}}\Delta\gamma\right)\right)(-b) \tag{C.18}$$

where b is the material coefficient as adopted in the reverse loading evolution Eq. (32). $\overline{\beta}_l$ is the backstress from the last branch of loading as defined in Eq. (34).

The above elastoplastic consistent tangent operators have been implemented in the Abaqus Umat subroutine for the proposed model.

Appendix D. Tables of parameters

Table D.1 presents the curve fitting results of ν_T and δ_T for every 100 °C. Linear interpolation will be used to obtain the intermediate values.

Table D.1
Least square fitting results for hardening law - EC3 carbon steel.

Temperature (°C)	ν_T	δ_T	Adj-R-sq
100	0.0	–	–
200	48.1	168.5	0.996
300	90.9	187.8	0.996
400	133.6	198.5	0.996
500	114.6	197.8	0.996
600	87.8	206.2	0.995
700	48.3	213.9	0.995
800	23.7	202.5	0.995
900	13.1	195.9	0.995
1000	8.9	196.1	0.995
1100	0.9	196.3	0.995

Table D.2
Least square fitting results - 304L stainless steel in Section 6.

Temperature	Hardening function			Bauschinger ratio evolution function			
°C	ν_T	δ_T	Adj-R-sq	a_T	b_T	c_T	Adj-R-sq
200	448.9	6.31	0.993	0.8504	184.5	0.1495	0.998
600	312.7	9.941	0.999	0.6996	189.3	0.3004	0.980
800	38.34	26.45	0.952	0.6786	267.2	0.3214	0.987
1000	1000.0	0.1003	0.977	0.9050	500.0	0.0943	0.974

Table D.3
Least square fitting results - low carbon steel in Section 7.

Temperature	Hardening function			Bauschinger ratio evolution function				Material parameter
°C	ν_T	δ_T	Adj-R-sq	a_T	b_T	c_T	Adj-R-sq	Vh_T
300	138.1	741.9	0.918	0.2212	5000.0	0.7781	0.996	1.45
700	19.22	1331.0	0.957	0.2801	4274.0	0.7100	1.0	1.45

Table D.4
Least square fitting results - 316 stainless steel in Section 9.

Temperature	Hardening function			Bauschinger ratio evolution function			
°C	ν_T	δ_T	Adj-R-sq	a_T	b_T	c_T	Adj-R-sq
650	13.5	1533.0	0.854	0.3078	800.0	0.70	1.0

References

[1] El-Rimawi J, Burgess I, Plank R. The treatment of strain reversal in structural members during the cooling phase of a fire. J Constr Steel Res 1996;37(2):115–35.
[2] Lamont S, Gillie M, Usmani A. Composite steel-framed structures in fire with protected and unprotected edge beams. J Constr Steel Res 2007;63(8):1138–50.
[3] Stern-Gottfried J, Rein G. Travelling fires for structural design -Part I: literature review. Fire Saf J 2012;54:74–85.
[4] Stern-Gottfried J, Rein G. Travelling fires for structural design-Part II: design methodology. Fire Saf J 2012;54:96–112.
[5] Dai X, Welch S, Usmani A. A critical review of “travelling fire” scenarios for performance-based structural engineering. Fire Saf J 2017;91:568–78.
[6] Dai X, Welch S, Usmani A. Structural implications due to an extended travelling fire methodology (ETFM) framework using SIFBUILDER. In: The 10th international conference on structures in fire; 2018.
[7] Institute SC. Structural fire engineering: investigation of broadgate phase 8 fire. Steel Construction Institute; 1991. ISBN 9781870004640.
[8] Ltd BRE. Results and observations from full-scale fire test at BRE cardington; 2003.
[9] Zhou M, Cardoso R, Bahai H, Usmani A. Thermo-mechanical behaviour of structural stainless steel frames in fire. In: The 10th international conference on structures in fire; 2018.
[10] DNV. Recommended practice: determination of structural capacity by non-linear FE analysis methods; 2013.
[11] Abambres M, Arruda MR. Finite element analysis of steel structures - a review of useful guidelines. Int J Struct Integr 2016;7(4):490–515.
[12] Lissenden CJ, Lerch BA, Ellis JR, Robinson DN. Verification of experimental techniques for flow surface determination. Tech. Rep.. National Aeronautics and Space Administration; 1996.
[13] Phillips A, Liu CS, Justusson JW. An experimental investigation of yield surfaces at elevated temperatures. Acta Mech 1972;14(2–3):119–46.
[14] Phillips A, Juh-Ling T. The effect of loading path on the yield surface at elevated temperatures. Int J Solids Struct 1972;8(4):463–74.
[15] Harley MBD, Miller EJ. Experimental study of internal variable evolution in SS304L at multiple rates and temperatures. J Eng Mater Technol 1999;121(2):162–71.
[16] Maciejewski K, Sun Y, Gregory O, Ghonem H. Time-dependent deformation of low carbon steel at elevated temperatures. Mater Sci Eng 2012;534:147–56.
[17] Ohno N, Yamamoto R, Okumura D. Thermo-mechanical cyclic hardening behavior of 304 stainless steel at large temperature ranges: experiments and simulations. Int J Mech Sci 2018;146–147:517–26.
[18] Franssen J. The unloading of building materials submitted to fire. Fire Saf J 1990;16(3):213–27.
[19] Franssen J-M, Gernay T. Modeling structures in fire with SAFIR : theoretical background and capabilities. J Struct Fire Eng 2017:JSFE–07–2016–0010.
[20] Eurocode 3 : design of steel structures - part 1–2: general rules - structural fire design; 2005.
[21] Franssen J-M. Safir: a thermal/structural program for modeling structures under fire. Eng J 2005;42(3):143–50.
[22] Elhami Khorasani N, Garlock MEM, Quiel SE. Modeling steel structures in OpenSees: enhancements for fire and multi-hazard probabilistic analyses. Comput Struct 2015;157:218–31.
[23] Mróz Z. On the description of anisotropic workhardening. J Mech Phys Solids 1967;15(3):163–75.
[24] Krieg RD. A practical two surface plasticity theory. J Appl Mech 1975;42(3):641.
[25] Dafalias YF, Popov EP. Plastic internal variables formalism of cyclic plasticity. Mech Res Commun 1976;3(1):33–8.
[26] Lee M-G, Kim D, Kim C, Wenner M, Wagoner R, Chung K. A practical two-surface plasticity model and its application to spring-back prediction. Int J Plast 2007;23(7):1189–212.
[27] Cardoso RP, Yoon JW. Stress integration method for a nonlinear kinematic/isotropic hardening model and its characterization based on polycrystal plasticity. Int J Plast 2009;25(9):1684–710.
[28] Prager W. The theory of plasticity: asurvey of recent achievements. Proc Inst MechEng 1955;169(1):41–57.
[29] Ziegler H. A modification of Prager’s hardening rule. Q Appl Math 1959;17(1):55–65.
[30] Chaboche JL, Rousselier G. On the plastic and viscoplastic constitutive equations -part ii: application of internal variable concepts to the 316 stainless steel. J Press Vessel Technol 1983;105(2):159.
[31] Chaboche J. Time-independent constitutive theories for cyclic plasticity. Int J Plast 1986;2(2):149–88.
[32] Chaboche J. A review of some plasticity and viscoplasticity constitutive theories. Int J Plast 2008;24(10):1642–93.
[33] Frederick C, Armstrong P. A mathematical representation of the multiaxial Bauschinger effect. Tech. Rep.; 1966.
[34] de Souza Neto EA, Peri D, Owen DRJ. Computational methods for plasticity : theory and applications. Wiley-Blackwell; 2008. ISBN 9780470694527.
[35] Drysdale D. An introduction to fire dynamics. Wiley; 1999.
[36] Armen H. Assumptions, models, and computational methods for plasticity. Comput Struct 1979;10(1):161–74.
[37] Rebelo N, Kobayashi S. A coupled analysis of viscoplastic deformation and heat transfer -I: Theoretical considerations. Int J Mech Sci 1980;22(11):699–705.
[38] Rebelo N, Kobayashi S. A coupled analysis of viscoplastic deformation and heat transfer -II: applications. Int J Mech Sci 1980;22(11):707–18.
[39] Kim J-H, Kim S-K, Lee C-S, Kim M-H, Lee J-M. A constitutive equation for predicting the material nonlinear behavior of aisi 316l, 321, and 347 stainless steel under low-temperature conditions. Int J Mech Sci 2014;87:218–25.
[40] Sun Y, MacIejewski K, Ghonem H. Simulation of viscoplastic deformation of low carbon steel structures at elevated temperatures. J Mater Eng Perform 2012;21(7):1151–9.
[41] Bushnell D. A strategy for the solution of problems involving large deflections, plasticity and creep. Int J Numer Methods Eng 1977;11(4):683–708.
[42] Nyssen C. An efficient and accurate iterative method, allowing large incremental steps, to solve elasto-plastic problems. Comput Struct 1981;13(1):63–71.
[43] Sloan S. Substepping schemes for numerical integration of elastoplastic stress strain relations. Int J Numer Methods Eng 1987;24:893–911.
[44] Marques J. Stress computation in elastoplasticity. Eng Comput 1984;1(1):42–51.
[45] Rice J, Tracey D. Computational fracture mechanics. In: Fenves SJ, editor. Numerical and computer methods in structure mechanics; 1973. p. 585–623.
[46] Ortiz M, Popov EP. Accuracy and stability of integration algorithms for elastoplastic constitutive relations. Int J Numer Methods Eng 1985;21(9):1561–76.
[47] Wilkins M. Calculation of elastic-plastic flow. University of California Lawrence Radiation Laboratory; 1963.
[48] Krieg RD, Krieg DB. Accuracies of numerical solution methods for the elastic-perfectly plastic model. J Press Vessel Technol 1977;99(4):510.
[49] Simo J, Govindjee S. Exact closed-form solution of the return mapping algorithm in plane stress elasto-viscoplasticity. Eng Comput 1988;5(3):254–8.
[50] Ortiz M, Simo JC. An analysis of a new class of integration algorithms for elastoplastic constitutive relations. Int J Numer Methods Eng 1986;23(3):353–66.
[51] Lush A, Weber G, Anand L. An implicit time-integration procedure for a set of internal variable constitutive equations for isotropic elasto-viscoplasticity. Int J Plast 1989;5(5):521–49.
[52] Yoon J, Yang D, Chung K. Elasto-plastic finite element method based on incremental deformation theory and continuum based shell elements for planar anisotropic sheet materials. Comput Methods Appl Mech Eng 1999;174(1):23–56.
[53] Design manual for structural stainless steel; 2018.
[54] Hill R. The mathematical theory of plasticity. Oxford University Press; 1998. ISBN 9780198503675.
[55] Inoue T, Tanaka K. Subsequent yield conditions of metal under cyclic loading at elevated temperature. Ingenieur-Archiv 1975;44(2):53–62.
[56] Nagtegaal JC. On the implementation of inelastic constitutive equations with special reference to large deformation problems. Comput Methods Appl Mech Eng 1982;33(1):469–84.
[57] Simo J, Taylor R. Consistent tangent operators for rate-independent elastoplasticity. Comput Methods Appl Mech Eng 1985;48(1):101–18.
[58] SIMULIA. Abaqus 6.14 user subroutine reference guide.
[59] Reverse yield experiments and internal variable evolution in polycrystalline metals. Int J Plast 1999;15(1):93–117.
[60] Ellis JR, Robinson DN, Pugh CE. Time dependence in biaxial yield of type 316 stainless steel at room temperature. J Eng Mater Technol 1983;105(4):250–6.
[61] SIMULIA. Abaqus 6.14 benchmarks manual.
[62] Clifton C. Fire models for large firecells. Tech. Rep. HERA; 1996.
[63] Rein G, Zhang X, Williams P, Hume B, Heise A. Multi-storey fire analysis for high-rise buildings. In: The 11th international conference and exhibition on fire science and engineering; 2007.
[64] Eurocode 1 : actions on structures; 2013.
[65] Silvestre E, Mendiguren J, Galdos L, de Argandona ES. Comparison of the hardening behaviour of different steel families: from mild and stainless steel to advanced high strength steels. Int J Mech Sci 2015;101–102:10–20.
[66] Dodds RH. Numerical techniques for plasticity computations in finite element analysis. Comput Struct 1987;26(5):767–79.